

Unterschrift des Betreuers



TECHNISCHE
UNIVERSITÄT
WIEN

Diplomarbeit

Influence of Ion Sputtering on Iron-Tungsten Alloy Surfaces and Iron Surfaces

Ausgeführt am Institut für
Angewandte Physik
der TECHNISCHEN UNIVERSITÄT WIEN

unter der Anleitung von

Univ.-Prof. Mag.rer.nat. Dipl.-Ing. Dr.techn. Friedrich Aumayr
und
Ing. Dipl.-Ing. Reinhard Stadlmayr, BSc.

durch
Dominic Blöch, BSc
Abelegasse 28/5
1160 Wien

Datum

Unterschrift Student

Kurzfassung

Treffen Ionen oder Atome auf feste Oberflächen, so kann eine ganze Reihe von Phänomenen auftreten. Als Beispiel seien hier die Emission von Photonen oder Sekundärteilchen, sowie die Implantation von Teilchen, etc genannt.

Ein besonders interessanter Effekt ist auch die Erosion von Oberflächen aufgrund von Zerstäubung, mit welchen sich diese Arbeit im Detail beschäftigt.

Beim Zerstäubungsprozess werden die obersten Atomlagen von der Oberfläche weggesprengt.

Das Abtragen geschieht dabei willkürlich, die Erosion ist also nicht überall auf der Oberfläche exakt gleich stark, was zu einer Veränderung der Oberflächenzusammensetzung und somit auch zu einer Veränderung der Erosionsgeschwindigkeit führt. Manchmal wird durch diese Modifikationen die Bildung von Strukturen auf der Oberfläche induziert. Sind diese quasi-periodisch können sie als Wellen bezeichnet werden.

Einerseits kann dieser Effekt durchaus erwünscht sein, so z.B. in der Halbleiter-Industrie, andererseits stellen sie oft ein großes Problem dar, wie z.B. bei der Erosion von Plasma-Komponenten in Fusionsanlagen.

In Fusionsanlagen sind die Plasma-Wand Interaktionen ein ungewolltes Phänomen. Die Belastung der Plasma-Komponenten durch den Ionenbeschuss führt zu einer Verkürzung der Lebenszeit der Komponenten. Ein gutes Verständnis von Plasma-Wand Wechselwirkungen ist daher essentiell, um die Lebenszeit von Fusionsanlagen zu verbessern.

Aus diesem Grund werden in dieser Arbeit Plasma-Wand Wechselwirkungen unter kontrollierten Laborbedingungen untersucht.

Hierbei kommt eine Quartz-Kristall-Mikrowage (QCM) Technik zum Einsatz. Mit dieser ist es möglich, auch kleinste Massenänderungen unter Ionenbeschuss nachzuweisen.

Letztendlich verfolgt diese Arbeit zwei Ziele. Erstens wird die Oberflächenanreicherung von schweren Elementen in Legierungen untersucht. Es wird dafür eine Eisen-Wolfram Legierung (98.5 at% Eisen 1.5 at% Wolfram) mit D_2^+ -Ionen beschossen. Diese Art der Legierung stellt ein Modell-System für den EUROFER-Stahl dar, welcher in zukünftigen Fusionsanlagen in abgelegenen Gebieten zum Einsatz kommen könnte. Durch einen Prozess, der bevorzugtes Zerstäuben genannt wird, wird in dem Fall Wolfram an der Oberfläche angereichert. Da Wolfram bessere Eigenschaften als Eisen in Bezug auf Anwendbarkeit in Fusionsanlagen besitzt, könnte eine Eisen-Wolfram-Legierung zukünftig als günstige Alternative zu reinem Wolfram verwendet werden.

Das zweite Ziel dieser Arbeit ist, den Wissensschatz bezüglich Quasi-periodischer Oberflächenstrukturen, wie Wellen, zu erweitern. Hierbei stehen besonders ihr Entstehungszeitpunkt und ihre Wirkung auf Zerstäubungsprozesse im Vordergrund. Zu diesem Zweck werden mit Eisen beschichtete Proben in mehreren Schritten mit Ar^+ -Ionen bestrahlt. Die Proben werden anschließend nach jedem Schritt mithilfe eines Rasterkraftmikroskops auf das Erscheinen von Wellen untersucht.

Abstract

When ions/atoms hit solid surfaces, a large variety of phenomena occur, e.g. the emission of photons, secondary particle emissions, the implantation of particles, etc.. One very interesting effect is the surface erosion due to sputtering. In the process of sputtering the first few atomic layers of the surface are removed. Since atoms at the surface are randomly sputtered, the erosion is not constant over the whole surface. This, in consequence, leads to surface modification, which results in an altered erosion rate. Sometimes this modification can lead to the formation of actual structures on the surface, often these structures can be described as quasi-periodic. In this connection they are called ripples. On the one hand, all these effects can be desired (e.g. semiconductor industry), on the other hand these phenomena can lead to serious consequences (e.g. erosion of plasma-facing-components (PFCs) in a fusion device).

In a fusion device, erosion of PFCs is an unwanted side effect. It reduces the lifetime of the components. Therefore, gaining a better understanding of plasma-wall-interactions is crucial for the lifetime and durability of future fusion devices. In this work, plasma-wall-interaction processes are studied under controlled laboratory conditions. The Quartz Crystal Microbalance (QCM) technique is used to measure the slightest mass changes of target layers, deposited onto the QCM crystal during irradiation with ions.

Two different goals are pursued in this work. The first one is the investigation of surface enrichment of high- Z elements in alloy materials. Here, the target material is an iron-tungsten alloy (98.5 *at%* iron and 1.5 *at%* tungsten) which is irradiated by D_2^+ ions. The reason why this iron-tungsten alloy was used is that it represents a model system for the EUROFER steel. EUROFER steel is currently being investigated for its applicability in recessed areas in future fusion devices. Through a process called preferential sputtering the surface is enriched with -in this case- tungsten. Since tungsten surfaces are much more suitable as PFCs than iron, tungsten containing steels like EUROFER could be a cheaper alternative to a pure tungsten coating in a fusion device. The second goal is to gain a better understanding of when the formation of quasi-periodic surface structures (like ripples) starts, as well as their influence on sputter processes. Therefore, pure iron coated samples are irradiated by Ar^+ ions in several fluence steps. Afterwards, investigations under an Atomic Force Microscope (AFM) are carried out, in order to monitor the formation of surface structures.

List of publications

Some of the results presented in this thesis have been presented in posters and/or published in scientific journals.

Publications

- Berger B. M., Stadlmayr R., Blöch D., Gruber E., Sugiyama K. Schwarz-Selinger T., Aumayr F.,
"Erosion of Fe-W model systems under normal and oblique D ion irradiation"
Submitted to Numerical Methods in Engineering

Poster presentations

- Blöch D., Stadlmayr R., Berger B. M., Kaser S., Bergen L., Aumayr F.,
"Sputtering of Fe surfaces by D and Ar ions",
12th European Conference for Atoms, Molecules and Photons 2016, Frankfurt am Main/Germany

Publications - non related

- Jericha E., Gösselsberger C., Bacak M., Baumgartner, S., Berger B., Blöch D., Gergen R., Hawlik A., Hinterleitner B., and Raab R.
Tailoring of polarised neutron beams by means of spatial magnetic spin resonance.
at the Joint Annual Meeting of the Austrian Physical Society and the Swiss Physical Society September 2013

Supervised students

- **Bernd Stechauner** - Bachelor Student
Ionen induzierte Erosion von Gold und Eisen Oberflächen.
from September 2016 until December 2016

Contents

Abstract	I
List of publications	IV
1 Introduction	1
1.1 Nuclear Fusion - a short overview	2
1.1.1 Nuclear fusion concepts	4
1.2 Motivation	6
1.2.1 FeW model systems surfaces	7
1.2.2 Fe surfaces	8
2 Sputter processes	9
2.1 Physical sputtering	9
2.1.1 Preferential sputtering	11
2.2 Surface modification due to sputter processes	12
2.2.1 Bradley-Harper theory	13
2.3 Computer simulations	15
3 Experimental methods	16
3.1 Setup for measuring small mass changes	16
3.1.1 Main parts of the setup	16
3.1.1.1 Vacuum chamber	16
3.1.1.2 Ion gun with deflection plates	18
3.1.1.3 The Quartz Crystal Microbalance (QCM)	19
3.2 Modified setup with aperture	20
3.3 Sputter yield measurements	21
3.3.1 The used samples	22
3.3.2 The QCM measurement device	23
3.3.3 Setting up the setup	24
3.3.4 Measuring procedure	24
3.3.5 Calculating the sputter yield	27

Contents

4	Experimental results	29
4.1	$D_2^+ \rightarrow FeW$	29
4.1.1	High fluence measurements	29
4.1.2	Short time angle dependent measurements	31
4.2	$Ar^+ \rightarrow Fe$	34
4.2.1	High fluence measurements	35
4.2.2	Angle-dependent measurements	37
4.2.3	Fluence step measurements with aperture	37
4.3	Discussion	41
5	Conclusion	48
	Bibliography	VII
	Danksagung	X



Chapter

Introduction **1**

Today, fossil power sources like oil, gas and coal as well as nuclear fission are the main suppliers to the electric energy needs of society [1]. Especially coal is by far the largest contributor to electric energy generation, with a contribution of nearly a third of the total world electric energy output. In the last decades the demand for electricity has grown more than the demand for any other form of energy. The IEA (International Energy Association) predicts a growing demand of $\sim 2.2\%$ per year until 2035. The worlds electric energy consumption was $\sim 19 TWh$ in 2011. This will make a total electric energy consumption of $\sim 32 TWh$ by the end of 2035 [1]. Although renewable electric energy sources are pushing forward, the demand for energy from fossil sources is increasing nonetheless. The main disadvantages of fossil power sources are firstly the CO_2 emissions, which leads to an increased greenhouse effect and secondly the diminishing of fossil reserves in the next centenary [1].

In the last decades renewable energy sources like photo-voltaic and wind-mill power plants have been subsidized by numerous countries but they are not capable of supplying the world energy needs [1]. In 1942 the first nuclear fission reactor was build (Chicago pile one) by Enrico Fermi during the top secret WWII "Manhattan Project" [2]. Since then nuclear fission has become a big contributor to the world electric energy production. The main advantages are the CO_2 emission free production process and the energy output per ton of fuel. One ton of Uranium-235 equals 2.7 *Mt* tons of coal in terms of energy production. However, at least since the nuclear incident in Chernobyl in 1986 the bright light of fission power sources has been overshadowed. The nuclear fall out from Chernobyl spread over Europe and lead to health risks for people going outside. Until today the near reactor region is highly contaminated with decay products from the incident. In addition, the deposition of nuclear waste still remains a problem regarding politics as well as the environment. No government wants the waste to be stored in their country and no government can assure the deposits remain safe for the next few thousands years, until the radioactive waste has decayed to the point where it is safe enough to be handled.

In the last few decades a new possible power source has been introduced, the nuclear fusion. Instead of uranium or plutonium, deuterium and tritium are used as fuel. The advantages of using these are that deuterium is naturally abundant in e.g. water and tritium can be produced out of lithium during a neutron capture process,



The abundance of deuterium in water (H_2O) is 0.0115% which ensures a sufficient supply for thousands of years. Lithium (out of which tritium can be produced) is naturally abundant in the earth crust, with an abundance of 0.006%, which is as abundant as tungsten¹ [3].

While it is true that tritium is radioactive and decays in a β^- process to ${}^3\text{He}$ with a lifetime of approximately 12.3 years,

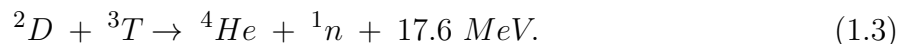


Additionally, only a few grams of tritium are needed to power a fusion device, instead of the several hundred kilograms uranium used in a fission device.

A big issue with fusion devices is the radioactive waste, which is produced during operation like in ordinary fission devices. Since there is a large variety of materials, which can be used in a fusion device, the waste can be reduced to a minimum by choosing the right materials. Today tungsten and beryllium are the choices, these materials do get activated during operation of the fusion device. But the resulting radioactive waste is "just" medium level waste, with a relatively short half-life [4], it diminishes so significantly after a few years, that the resulting materials could be recycled for use in other fusion devices. Today's research (like this work) is also aiming for new materials, which can be used in a fusion device. A steel called EUROFER [5] is currently under investigation for its applicability in fusion devices as plasma facing material in recessed areas of the device. Due to its composition, this steel (mainly iron with a few higher- Z elements like tungsten) is a low-activation steel and therefore a good choice for application in fusion devices.

1.1 Nuclear Fusion - a short overview

Fusion is a nuclear process in which two or more atom nuclei merge to build a different atom, like deuterium and tritium which merge (fuse) to helium



¹Uranium-235 has an abundance of less than $10^{-5}\%$.

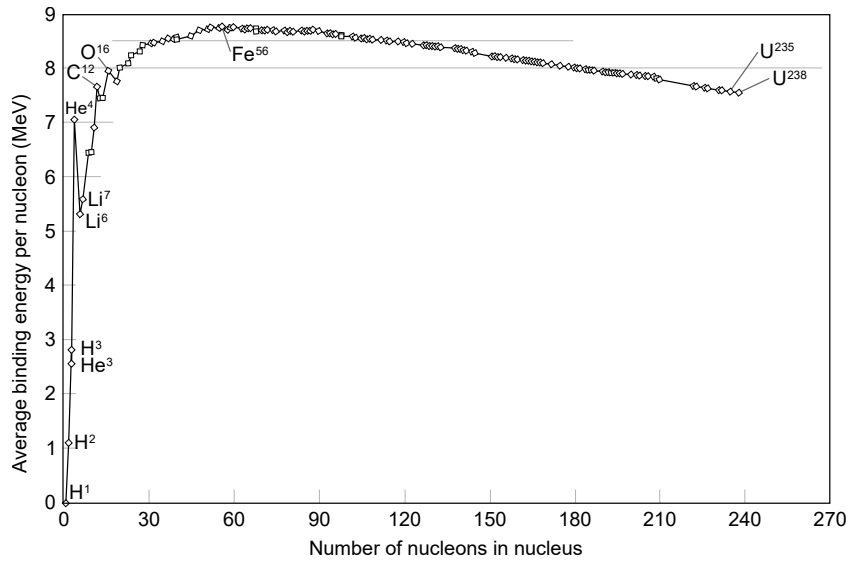
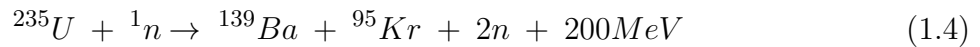


Figure 1.1: Binding energy per nucleon for different isotopes. [7]

In the displayed process an additional neutron as well as a great amount of (kinetic) energy are set free. In total 17.6 MeV , 3.5 MeV for the helium and 14.1 MeV for the neutron. In order to calculate the energy balance of such a process it is necessary to estimate the binding energy of the nuclei before and after the process. This can be achieved via the Bethe-Weizsäcker formula [6], which calculates the total binding energy of nuclei. This energy divided by the number of nucleons gives the binding energy per nucleon, which is the usually desired quantity. In figure 1.1 the binding energy per nucleon is displayed for a large variety of isotopes. It features a maximum at approximately ${}^{56}\text{Fe}$. This means that atoms lighter than ${}^{56}\text{Fe}$ can be fused and atoms heavier than ${}^{56}\text{Fe}$ can be used to gain energy via fission processes. With the help of this figure it is possible to calculate the total energy gain of a process by simply calculating the binding energy before and after the process. For a possible fission process of Uranium-235 like:



a total energy gain of 200MeV can be calculated². So why bother with fusion if at first glance, fission releases more energy per reaction? Consider one gram of Uranium-235 and one gram of a deuterium-tritium mixture. If this uranium completely fissions into its daughter nuclei (e.g. ${}^{139}\text{Ba}$ and ${}^{95}\text{Kr}$) a total energy of $\sim 82 \text{ GJ}$ is released. One gram of the deuterium-tritium mixture on the other hand releases $\sim 336 \text{ GJ}$. Therefore, the fusion of one gram deuterium-tritium mixture releases approximately four times as much energy as fission of one gram Uranium.

²While other decays are possible, the reaction displayed in equation 1.4 is the most likely.

1.1.1 Nuclear fusion concepts

As mentioned before, any energy production from nuclear reactions is based on the different nuclear binding energy of the involved nuclei. The explanation for the structure in figure 1.1 is as follows. All reactions considering nuclear reactions are usually governed by the strong interaction, which holds the protons and neutrons together in the nuclei. This interaction is very short ranged, only $10^{-15} m$ [8], thus the constituents of the nuclei influence only their nearest neighbors. This would mean a constant binding energy per nucleon. The small binding energy per nucleon for small nuclei is due to the relatively large surface to volume ratio. The nucleons at the surface therefore lack a partner and thus their contribution to the binding energy is reduced. For higher- Z nuclei ($A \approx 60$) the decrease in the binding energy is caused by the repulsive force of the large amount of protons.

Beyond the range of the strong interaction the Coulomb force of the protons is the dominant force. This prevents other nuclei of getting too close to each other and therefore from fusing. Only at sufficiently high energies (temperatures) the nuclei can come close enough, so that the probability that one nuclei tunnels through the Coulomb wall into the other nucleus and fuse is high enough. After the tunneling the attractive strong interaction becomes the dominant force and the nucleons from both nuclei form a new nucleus. In figure 1.2 the schematics of such a reaction is displayed. The probability for fusion of two nuclei is therefore dependent on the probability of tunneling. The tunneling probability is a function of the relative velocity (temperature) v and the charge of both particles Z_1 & Z_2 .

$$P_{tunneling} \sim \exp\left[-\frac{2\pi Z_1 Z_2 e^2}{\hbar v}\right] \quad (1.5)$$

Gravitational confinement

The sun is doubtlessly the best example of fusion and also the best way to describe gravitational confinement. Due to the high mass of the sun, the gravitation in its core -which is around 1/64 of the volume of the sun and contains $\sim 25\%$ of the solar mass- is 220 times higher than earth gravitation. In this region a temperature of $15.7 MK$ and pressure of $247 Gbar$ are prevalent [9]. These conditions make it possible for nuclei to fuse. The total energy output of the sun approximately measures $3.846 \cdot 10^{26} W$ [9].

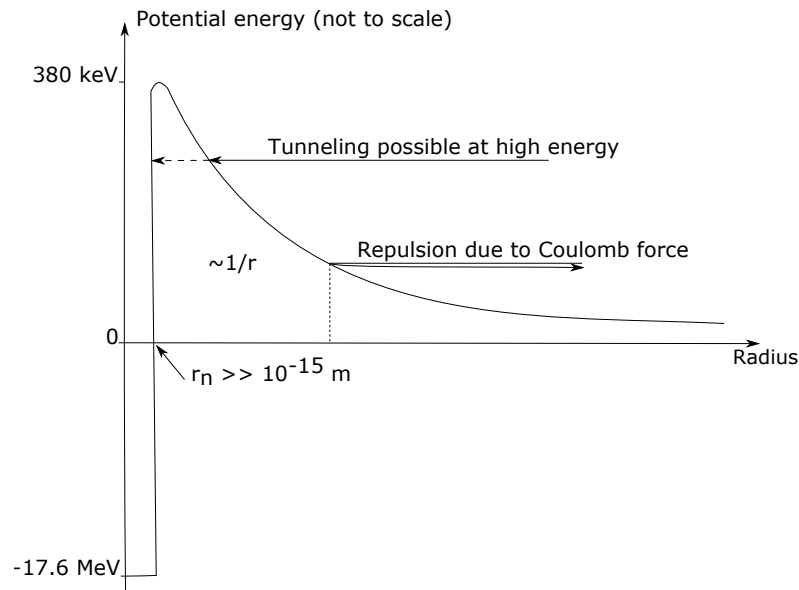
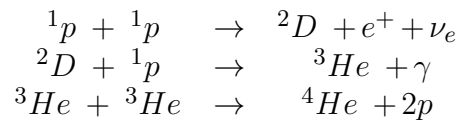


Figure 1.2: Schematics of the potential energy between a deuterium and a tritium nucleus colliding as a function of their distance. At high energies, tunneling of one nucleus into the other is possible. At lower energies, repulsion takes place.

The main reaction cycle is the following:



and it is called the pp-cycle [10].

An important feature of the first reaction is, that it needs the weak interaction, which transforms one proton over a β^+ -decay into one neutron. Thus, the reaction involves the emission of a neutrino, in order to conserve the lepton number. This reaction occurs rather rarely. This explains the long lifetime of the sun, since the sun mainly consists of protons.

Inertial confinement

Inertial confinement is a fusion concept in which the fuel is irradiated by highly intense LASERs or particle currents from all directions in order to assure a homogeneous, inwards directed pressure. Through this the fuel compresses and the pressure and temperature increase drastically. In this state the fuel "burns down" in just a few nanoseconds and it is held together by the inertia of masses.

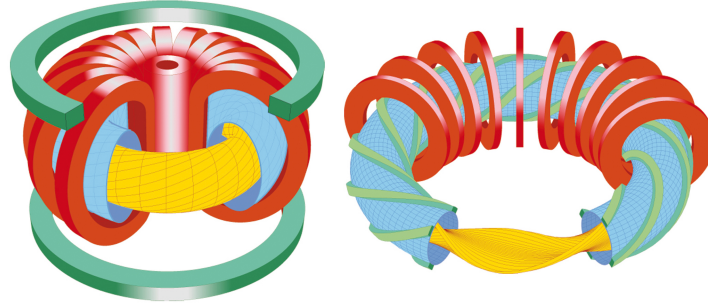


Figure 1.3: Left: Tokamak concept. Right: Stellarator concept. [11]

This fusion concept is mainly pursued by the United States of America (USA). The most successful facility using this concept is the American National Ignition Facility (NIF).

Magnetic confinement

The magnetic confinement concept is probably the most advanced fusion concept today. Within this concept the fuel is heated by microwaves and/or particle beams to a temperature of $10\text{-}20\text{ keV}/k_b$. To prevent the fuel plasma from drifting apart, strong magnetic fields are applied to compress the plasma. Today, two types of fusion device concepts are followed. The first type is called the Stellarator. The name is derived from the greek "stellar" - meaning sun - indicating that it produces energy just like the sun. The second type is the TOKAMAK, named for a Russian acronym translating to "toroidal chamber with magnetic coils" [11]. Both use magnetic fields to achieve the confinement of the plasma. However, the concepts behind them are completely different and would exceed the scope of this thesis. For a profound explanation of these two fusion device types, see [12]. In figure 1.3 the schematic views of a Stellarator and a Tokamak are shown.

1.2 Motivation

Although a lot of progress has been made in fusion research in the last decades, a lot of technical issues still need to be solved in order to achieve a stable and safely functioning fusion device. For example, the inner coating of a fusion reactor, which faces the hot plasma, is constantly bombarded by ions. It is one of the most stressed parts in a fusion device. Therefore, it is crucial to understand plasma-wall interactions.

Due to this ion bombardment the inner coating of the reactor is sputtered and in consequence the plasma is contaminated with wall material, which in turn is ionized by impact ionization. These ions join the fusion plasma and usually cool the plasma, which in turn leads to a poorer fusion process and the necessity of more heating power. Also, the lifetime of the plasma facing components is limited by the erosion rate due to ion bombardment. It is therefore preferable to use materials which sustain the ion bombardment.

In this thesis, the impact of deuterium ions on iron-tungsten (FeW) alloys and Argon ions on pure iron are investigated under different angles of incidence. The interaction of the ions with surfaces in the laboratory setup should be comparable to the plasma-wall reactions in a fusion device. The deuterium ions have a kinetic energy of $250 \text{ eV}/D$ and a total fluence of $\sim 3 \cdot 10^{23} \text{ D}/m^2$ is applied to each sample. The Argon ions have an energy of $500 \text{ eV}/Ar$ and the applied fluence is $\sim 6.8 \cdot 10^{23} \text{ Ar}/D$. Furthermore, Atomic Force Microscope (AFM) investigations have been performed before and after irradiation to show nano-sized surface modifications of the surfaces due to the sputtering processes.

1.2.1 FeW model systems surfaces

As mentioned before, tungsten is a possible candidate for the coating of plasma facing components in future fusion devices. It provides good sustainability against high heat fluxes and the constant ion bombardment. However, tungsten is brittle at room temperature and its thermal and mechanical conjunction in the fusion device during construction can be challenging. In order to reduce both technical effort and costs, using steels containing small amounts of high-Z elements like tungsten in recessed areas of a fusion device can be an attractive alternative. Tungsten containing steels, such as EUROFER [5], are tougher than pure tungsten. Since EUROFER mainly consists of iron, mostly iron is sputtered during irradiation. However, due to preferential sputtering (see chapter 2.1.1) of medium-Z steel elements, the surface is enriched with higher-Z elements like Tungsten, which reduces the erosion yield considerably (compared to a pure iron surface). This, in turn, increases the lifetime of the components.

In this work an iron-tungsten films (98.5 at% iron and 1.5 at% Tungsten) is used instead of the EUROFER steel. It represents a model system for the EUROFER steel. This steel is irradiated by mono-energetic (250 eV) deuterium ions under different angles of incidence, while the mass removal is constantly measured in order to investigate the influence of high-Z element-surface enrichment on the mass removal rate. The energy of $250 \text{ eV}/D$ is chosen because it is at around the sputter threshold of tungsten. This increases the influence of preferential sputtering (see section 2.1.1) on the sample and therefore accelerates the surface enrichment of high-Z elements. In Chapter 4 the results of these measurements are presented.

1.2.2 Fe surfaces

When a surface is bombarded by ions, the previously mentioned sputter process starts. This also leads to a large variety of surface modifications. These modifications can build either chaotic structures leading to a surface roughening or quasi-periodic structures, depending on the material and the angle of incidence as well as the surface itself. In order to have clean conditions for monitoring surface modifications during irradiation, it is necessary to get rid of effects like preferential sputtering and the influence of initially present surface structures. Therefore, only polished surfaces and pure element samples are used.

In this work, polished and pure iron surfaces were irradiated by mono-energetic Argon ions (500 eV) under different angles of incidence, while the mass removal was measured with a QCM technique (see section 3.1.1.3). Argon is used since the measured signal improves due to its high mass, compared to deuterium. After certain fluence steps, AFM investigations were conducted to monitor surface structure formations. In Chapter 4 the results of these measurements are presented.

Sputter processes

2.1 Physical sputtering

When surfaces are hit by ions/atoms, the projectiles undergo collisions with the atoms of the target. In these collision processes the projectiles lose energy through elastic and/or inelastic scattering, which is transferred to the neighboring atoms on the surface. Usually, when the projectile penetrates the surface the projectile initiates a collision cascade. In a simple case this collision cascade can be approximated by several binary collisions. Assuming only elastic collisions, the energy transfer during the collision from one particle to the other is given by the energy and momentum conservation [13].

$$\begin{aligned} E_1^{kin,before} &= E_1^{kin,after} + E_2^{kin,after} \\ p_1^{before} &= p_1^{after} + p_2^{after} \end{aligned}$$

When a surface atom experiences a collision¹ and the transferred energy is higher than the surface binding energy of the surface atom, the surface atom can leave the surface, when the resulting momentum vector is outwards directed. In this case the process is called sputtering. The quantity usually used to measure sputtering is the sputter yield Y .

$$Y = \frac{\text{sputtered atoms}}{\text{projectile atom}} \quad (2.1)$$

For composite targets the sputter yield Y is usually not used, since in composite targets it can not always be determined which species of the target atoms is sputtered.

¹From the projectile particle or the collision cascade.

Therefore, the mass removal rate is used instead.

$$\text{Mass removal rate} = \frac{\text{mass}}{\text{projectile atom}} \quad (2.2)$$

Here it is irrelevant which atom is sputtered. The sputter yield and the mass removal rate are connected through a constant factor which depends on the composition and the masses of the involved materials. Henceforth, the mass removal rate is used within composite targets and the sputter yield for non-composite targets.

In order to calculate the minimum ion impact energy for a collision, which leads to sputtering, the above mentioned energy and inertia conservation laws can be applied. The maximum transferred energy from one projectile to the other is, when the projectiles collide frontally with each other [13]. This leads to an energy transfer of:

$$\Delta E_{kin}^{max} = \frac{4\mu^2}{m_1 m_2} E_1 \quad \text{with} \quad \mu = \left(\frac{1}{m_1} + \frac{1}{m_2} \right)^{-1}. \quad (2.3)$$

Where μ is the reduced mass, m_1 and m_2 are the masses of the two involved particles and E_1 is the kinetic energy of the projectile particle with mass m_1 -assuming that the target particle m_2 rests-.

Therefore, when two particles collide frontally and the transferred energy from equation 2.3 is higher than the surface binding energy of the surface atoms, sputtering is possible. In order to achieve this energy transfer the projectile particle must have a minimum kinetic energy of $E_{kin}^{min} = 0.5 \cdot m_1 v_1^2 = \Delta E_{kin}^{max}$. If the projectile atom has a kinetic energy greater than ΔE_{kin}^{max} , sputtering can even start when the two particles do not collide frontally. In figure 2.1 the sputter yield over the impact energy for deuterium hitting iron is displayed². It features a minimum energy for sputtering at $\sim 20 \text{ eV}/D$ and a maximum at $\sim 500 \text{ eV}/D$. Due to fact, that at high kinetic energies, the collision cascade spreads deeply into the bulk and therefore the energy deposition is in the bulk and less surface-near atoms gain enough energy to leave the surface. By increasing the impact angle -with respect to the surface normal- the collision cascade and therefore the energy deposition can be held closer to the surface, which in turn increases the sputter yield. In section 2.2.1 a more profound explanation for this phenomenon is given.

²The impact angle with respect to the surface normal is 0 degrees.

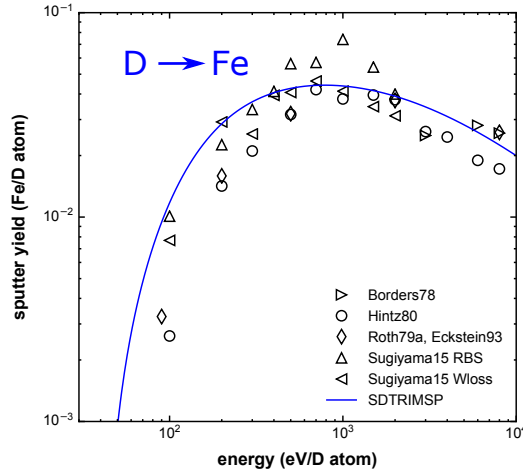


Figure 2.1: *D* on Fe. Sputter yield as a function of projectile impact energy. The symbols are measurements [14], the blue line a SDTrimSP simulation. The impact is perpendicular.

2.1.1 Preferential sputtering

If a target consisting of two different but homogeneously mixed materials (A and B) -the concentrations (c_a and c_b) of which add up to one- is irradiated by ions or fast atoms, materials A and B will be sputtered. Due to the fact that each material has its own sputter yield with respect to the projectile ions³ the materials are sputtered differently. If, for instance, material A has a higher sputter yield than material B, material A depletes faster from the surface⁴ and subsequently the surface concentrations of A and B change. During this process the overall sputter yield changes as well, due to the changed surface concentrations. After sufficiently long irradiation, the surface concentrations as well as the sputter yield will reach a steady state [14].

The following equation 2.4 describes the relationship between sputter yield and surface concentration in equilibrium.

$$\frac{Y_a}{Y_b} = \frac{c_a}{c_b} \quad (2.4)$$

Here, Y_a and Y_b are the respective partial sputter yields of the components A and B.

³In fact due to the composition of materials the surface binding energy for each atom species changes with the concentration as well.

⁴This effect is extremely pronounced when for instance the impact energy of the projectile particles is high enough to sputter B, but not A.

As mentioned before, in the initial stages of irradiation the composition of the sputtered material can deviate from the steady state case [14]. This alters the entire sputter yield compared to the steady state case. To generalize this, the ratio from equation 2.4 must be altered in order to describe the new situation. This leads to:

$$\delta = \frac{Y_a c_a}{Y_b c_b} \quad (2.5)$$

in which δ is the sputter preferentiality [15].

Usually, the sputter preferentiality is influenced by the chosen materials (i.e. their surface binding energy or mass) and their concentration in the bulk. However, as a rule of thumb most often the material with the lower mass is sputtered preferentially [15].

2.2 Surface modification due to sputter processes

When surfaces are irradiated by ions the previously mentioned sputtering happens. This process gives rise to a large variety of surface modifications, but mostly a simple roughening of the surface takes place. Under certain circumstances these modifications can form specific patterns on the surfaces. In some cases they can be described by quasi-periodic height modulations [16, 17]. This depends on the target materials, the crystallographic properties, the angle of incidence of impacting particles and other properties like the surface temperature.

When the ion beam hits the surface under oblique angle of incidence, two interesting types of patterns, also called ripples, can be observed. Perpendicular Mode Ripples (PeMR) and Parallel Mode Ripples (PaMR) [16]. The terms perpendicular and parallel correspond to the angle of the wave-vector of the ripples and the projection of the ion-beam on the surface. The Bradley-Harper theory [17] was one of the first mathematical descriptions of this phenomenon and will be explained in the following section.

2.2.1 Bradley-Harper theory

The Bradley-Harper theory [17] is a continuum model description of surface formations due to ion sputter processes based on the sputter theory of Peter Sigmund [18]. With this theory the erosion rate v can be calculated by:

$$v = p \int \phi(\mathbf{r}) E_d(\mathbf{r}) d\mathbf{r}. \quad (2.6)$$

Where \mathbf{r} is the stationary vector, $\phi(\mathbf{r})$ is the ion flux density, p is a proportionality factor between erosion rate and energy deposit in the surface due to ion bombardment and $E_d(\mathbf{r})$ is the spatial energy distribution of one ion in the surface. With this information Bradley and Harper found a partial differential equation which can describe the erosion rate of the surface $\partial h/\partial t$ as a function of the spatial derivation and the local curvature [17].

The Bradley-Harper equation successfully describes the roughening and smoothing of surfaces due to surface diffusion processes. It can also describe the two forms of ripple formations, PeMR and PaMR at oblique angle ion incidence. With the Bradley-Harper theory it is possible to calculate how much the surface topology changes with increasing fluence. It shows how an initially flat surface -with only small perturbations in the surface height- becomes rougher over time. This is due to how and where energy is deposited by ions in surfaces. The Bradley-Harper equation shows that the energy deposition of ions in the surface near region is higher in valleys than in apex regions. In figure 2.2 a schematic representation of this behavior can be seen. The gray scale indicates the energy density due to ion impact. The darker the area the higher the energy deposition. Therefore, more atoms are sputtered in the valleys because more atoms gain enough energy to leave the surface. This leads to an increase of the amplitude of surface structures and consequently to a higher roughness. As a result the local impact angle of the projectile material changes with the applied fluence and therefore so does the sputter yield, compared to a flat surface. This impact angle distribution also occurs on initially rough surfaces.

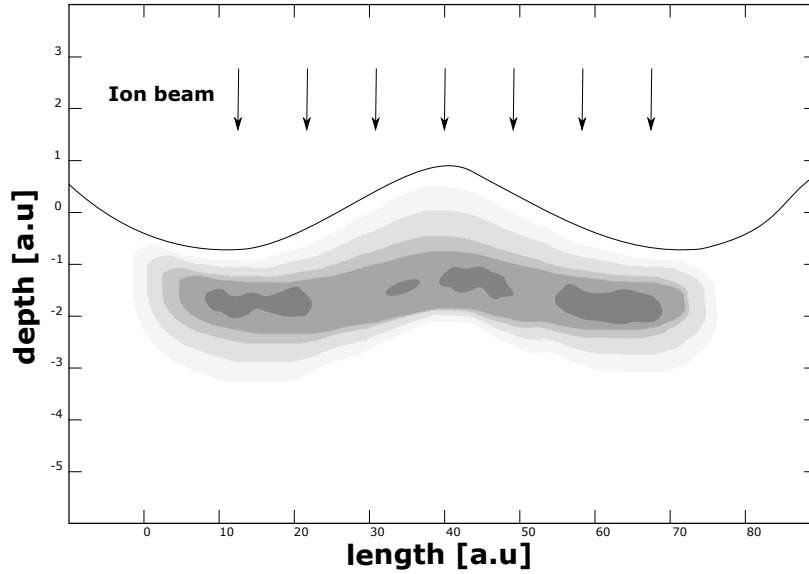


Figure 2.2: Schematics of the energy deposition in surfaces due to ion bombardment. The grey scale corresponds to the amount of deposited energy in the viewed area. It is clear to see that the energy density is higher in the valley than in the apex region. The impact angle with respect of the surface normal is 0 degrees.

The same arguments can be used to describe the angle dependency of the sputter yield. Ions which impact under oblique incidence deposit more energy in the surface-near regions which enables more atoms per impacting ion to actually leave the surface. On the other hand, ions which impact under perpendicular angle of incidence deposit their energy into the bulk. This enables only a few atoms to gain enough energy to leave the surface.

Although the Bradley-Harper theory successfully describes e.g. ripple formation, it lacks certain important features. In the theory an exponential growth of the amplitude of the ripples is predicted. In the early stages of irradiation this is indeed the case, but with progressing irradiation the exponential growth ceases [19].

The Kuramoto-Sivashinsky equation [20, 21] considers higher order derivations and can describe the observed phenomena more precisely.

2.3 Computer simulations

To gain a better understanding of sputter processes, computer simulations are of importance for this work, be it, to get a better understanding of ion surface interactions, or to compare the experimental results with the results calculated by computers.

In this work the software SDTrimSP version 5.07 was used [22]. This program is based on Trim.SP and TRIDYN [23–25], which are based on Monte Carlo simulations using a binary collision approximation (BCA) for each scattering process. This means that each projectile particle experiences multiple, separate collisions with the surface layer particles on its path through the surface layers⁵. Between collisions no other interaction occurs between particles. SDTrimSP assumes an amorphous target with infinite lateral extent. The target is divided into a finite number of layers. Depending on the input parameters, the target layer thickness and compositions can change during particle irradiation. With this program it is possible to calculate the sputter yield, reflection coefficients, transition coefficients, target composite changes, etc.. This allows the program to include effects such as preferential sputtering within its code.

SDTrimSP is a powerful program, nevertheless it lacks certain important features. It does not include the surface roughness in its calculations. Therefore, the influence of the surface roughness on the sputter yield is not included. This results in an inevitable error, when comparing calculated results with measured results.

⁵Scattered surface layer particles in turn can experience collisions as well with neighboring particles.

Chapter **3**

Experimental methods

3.1 Setup for measuring small mass changes

In the following sections a setup will be presented, which is capable of measuring very small mass changes. During this thesis the setup undergoes certain modifications to also be capable of investigating fluence-dependent surface structure formations, but still be capable of measuring the mass change due to ion bombardment.

3.1.1 Main parts of the setup

The used setup can be divided into three main parts:

- The vacuum chamber
- The ion gun with beam optics
- The Quartz Crystal Microbalance (QCM)

In the following sections these parts will be described. In figure 3.1 the whole setup is displayed with its parts marked by circled numbers.

3.1.1.1 Vacuum chamber

As in any surface physics experiment, it is important to have good vacuum conditions, in order to reduce ion beam density losses etc. during application. In this experiment a residual gas pressure of 10^{-7} to 10^{-9} *mbar* in the vacuum chamber is typical. At higher pressures ions could undergo collisions with the residual gas atoms and neutralize. The resulting neutral atoms can sputter material from the sample like ions could do.

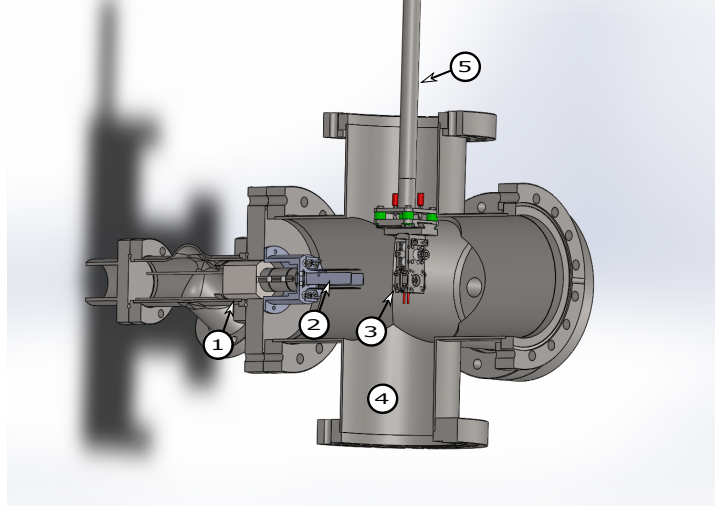


Figure 3.1: A CAD drawing of the used setup.

- ① Ion-gun
- ② Beam optics
- ③ QCM holder
- ④ Vacuum vessel
- ⑤ $xyz\phi$ -stage

But these neutralized ions can not be measured easily and compromise the ion current density measurement (see section 3.3.2), which is of crucial importance to this experiment.

In order to quantify collisions between gas atoms the so called mean free path λ should be considerably larger than the distance between ion-gun and sample. The connection between ion-gun to target distance d and the mean free path λ can be described by:

$$d \gg \lambda = \frac{1}{n \cdot \sigma}. \quad (3.1)$$

Where n is the density of atoms and σ the charge exchange cross section. For example, if the distance measures $\sim 10 \text{ cm}$ (like in this setup), a vacuum pressure should be better than 10^{-3} mbar . However, at ultra high vacuum conditions (like in the used setup) a pressure of 10^{-7} mbar leads to a mean free path of about 1 km , which is sufficient for these measurements with this setup.

However, the residual gas pressure should always be kept at its absolute possible minimum, whether or not 10^{-3} mbar would suffice. Due to electronic impact ionization of the residual gas atoms in the ionization chamber in the ion gun, residual gas atoms can be ionized. These impurity ions compromise the experiment by sputtering material from the sample with an "unknown" sputter yield.

While these impurity ions can not be measured directly, it is possible to measure the residual gas via a mass spectrometer¹. This way, the influence of the impurities can be estimated. One of these mass spectra is shown in figure 3.2. Here, the ion currents measured by a quadrupole mass spectrometer is shown. The working gas -in this case deuterium- was infused. The y-axis corresponds to the intensity of the corresponding masses shown on the x-axis. A clear peak at a mass of four amu is visible. This is the D_2^+ peak, which should be as high as possible, since it is the working gas. But besides the D_2^+ peak other peaks are visible. Mind that the scale of the y-axis is a logarithmic one, which means that the intensities of all other specimen is at least one (D_3^+) or several order of magnitude lower than that for D_2^+ . These are the impurity atoms in the vacuum chamber, which as mentioned before should be as low as possible.

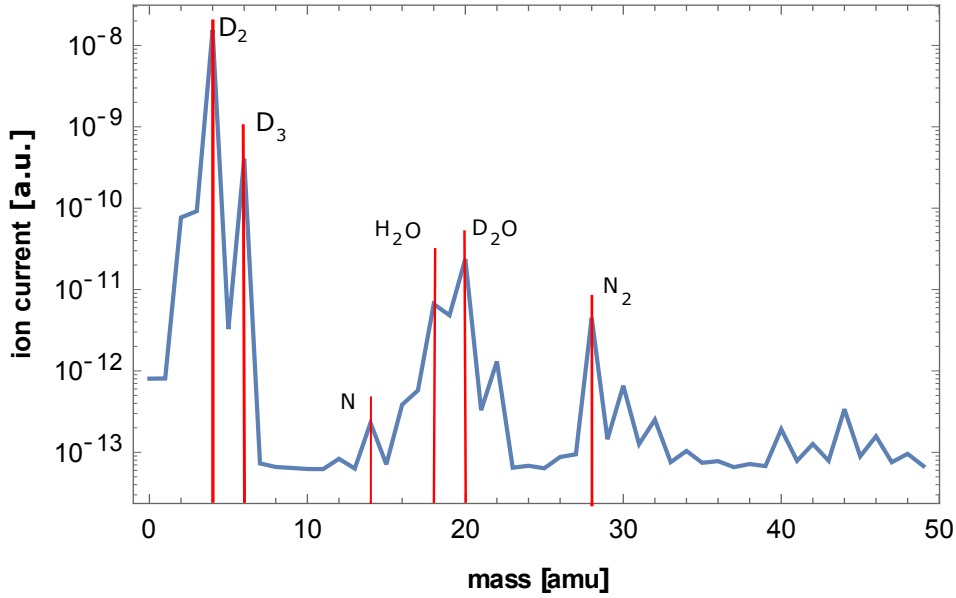


Figure 3.2: Residual gas spectrum measured at the target chamber. There are clear signs of impurity atoms/molecules, for instance nitrogen and water, but their intensities are a few permille at most.

3.1.1.2 Ion gun with deflection plates

The ion gun (type Perking Elmer PHI 04-261 2kV) used in this setup is an electron impact ionization source. Acceleration voltages up to 2000 V are possible. An Einzel-lens at the front end of the gun allows focusing the ion beam. In order to manipulate the ion beam, additional deflection plates have been added after the Einzel-lens.

¹In this experiment a quadrupole mass spectrometer was used.

Applying a voltage to them bends the ion beam in a desired direction. The ion gun, as well as the deflection plates can be seen in figure 3.1, points ① and ②.

3.1.1.3 The Quartz Crystal Microbalance (QCM)

In order to conduct sputter yield measurements, a QCM technique² is used [26, 27]. The QCM uses a quartz crystal which, is driven at its resonance frequency. The used crystals are stress compensated (SC-cut). On either side of the crystal, 100 nm thick gold electrodes are vapor deposited. These are necessary to ensure a good electric connection between the electronics, which drive the quartz crystal and the quartz crystal itself. The resonance frequency depends on the thickness of the quartz as well as on the thickness of (possibly) deposited materials. When surface materials (e.g. iron) are sputtered the resonance frequency of the crystal changes due to the changed thickness. This change in the frequency can be measured and gives information about the mass change of the sample. Sauerbrey [27] found a simple relation between mass change and frequency change, which can be described as:

$$\frac{\Delta f}{f} = -\frac{\Delta d}{d} = -\frac{\Delta m}{m} \quad (3.2)$$

As seen in equation 3.2, the frequency change is proportional to both thickness change and mass change. Due to a temperature dependency of the resonance frequency of quartz crystals [27], the crystals must be temperature stabilized. Each crystal has its own thermal minimum frequency [27], which it should preferably be driven at. For methods to calculate the actual mass removal due to a frequency change, see section 3.3.5.

In figure 3.3 the schematics of the QCM is shown. It displays the quartz crystal the electrodes plus an applied surface layer, which is sputtered by an ion beam under an angle of incidence α (measured from the surface normal). For more detailed informations about the QCM technique, see [26] and [27].

²This particular QCM technique was developed at the TU Wien.

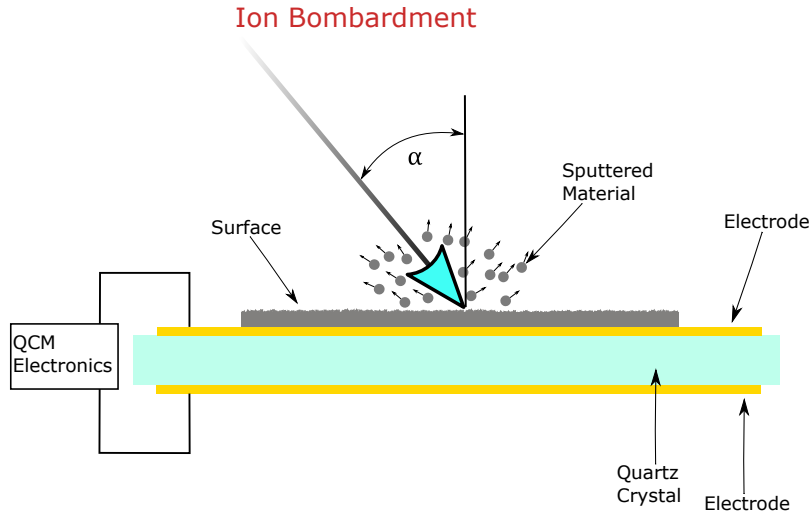


Figure 3.3: Schematics of the QCM. Due to ion bombardment, atoms of the target's surface are sputtered, resulting in a change of the crystals resonance frequency. The ion beam hits the surface under an angle of α .

3.2 Modified setup with aperture

In order to investigate the fluence dependency of surface structure formations like PeMR or PaMR (later to be inspected by AFM), the setup was improved with an additional aperture. This aperture allows application of different fluence steps to one sample without opening the vacuum vessel and changing samples. The aperture can be seen in figure 3.4, point ③. The aperture is rotatable, so that it can be completely retracted and the old setup configuration is accessible without any further modifications.

During measurements the QCM holder can be shifted via the $xyz\phi$ -stage (figure 3.4, point ⑥) in order to conceal parts of the sample which should not be irradiated. This way it is possible to irradiate the sample surface in fluence steps.

Aperture for relative ion current measurements

In addition, another aperture was added to monitor the ion current during measurements, which allows a qualitative statement about this current. This aperture was originally installed, in order to investigate the long-time stability of the ion beam of the ion-gun. In figure 3.4, point ① this aperture can be seen.

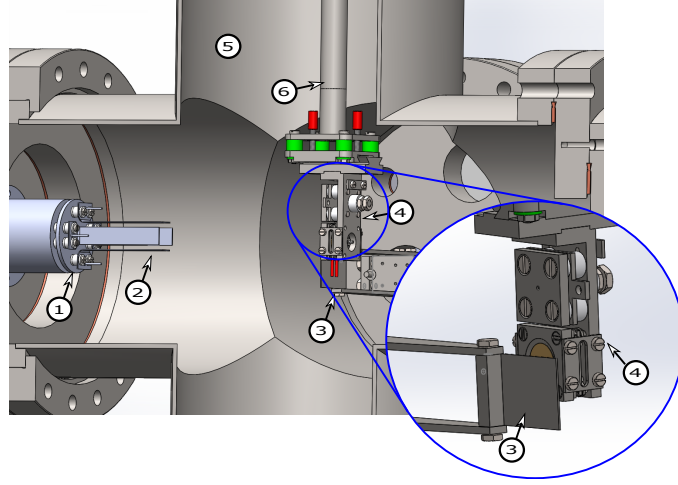


Figure 3.4: CAD drawing of the modified setup.

- ① Aperture for relative ion current measurements
- ② Deflection plates
- ③ Aperture for fluence step measurements
- ④ QCM device with Faraday Cup
- ⑤ Vacuum vessel
- ⑥ $xyz\phi$ -stage

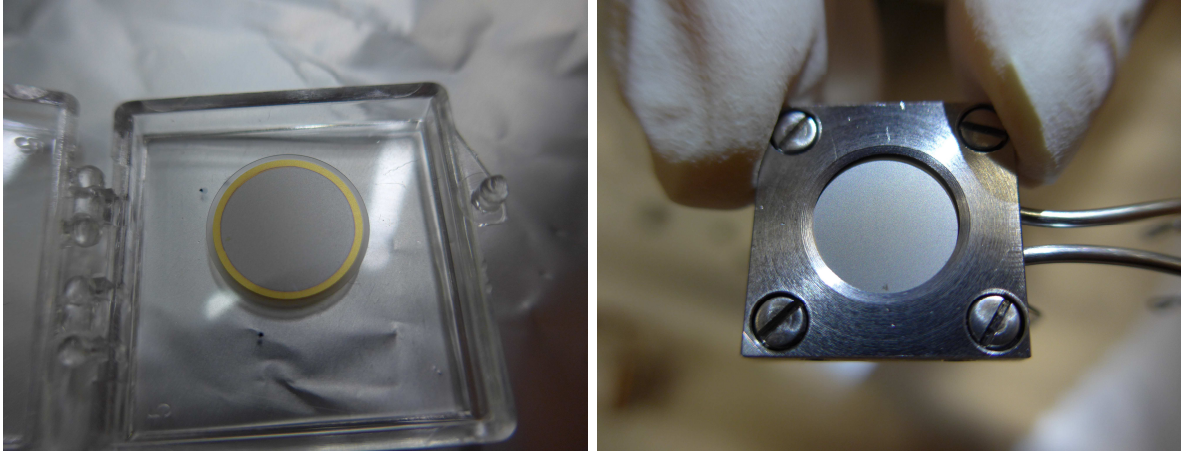
3.3 Sputter yield measurements

With the setup, irradiation angles up to 70 degrees from the sample surface normal are possible. This is acquired through the $xyz\phi$ -stage, seen in figure 3.4, point ⑥. All measurements shown here were done at an extraction voltage of 500 V. Furthermore, the temperature of the QCM holder was stabilized at approximately 430 K.

This experiment consisted of two different measurement series, each series featuring different projectile and target materials³. In one series deuterium ions are used as projectiles⁴. Since in fusion devices, deuterium and tritium will be used as fuel, using deuterium and tritium ions as projectiles would be wise. Unfortunately, tritium decays in a β^- process to helium and is a potential health risk, it was not possible to use it in. The other measurement series is done with argon as projectile material, in order to achieve larger signals and therefore clearer results. Since the argon sputter yield is much higher than the deuterium sputter yield, the signal on the QCM improves. Furthermore, impurity atoms in the residual gas does not effect the experiment as much as it would be the case with deuterium.

³Target materials will be explained in section 3.3.1.

⁴Deuterium is in use in research fusion devices like ASDEX Upgrade in Germany.



(a) QCM quartz crystal disc.

(b) QCM holder with quartz crystal disc.

Figure 3.5: (a): Photograph of the non-polished quartz crystal disc samples. (b): Quartz crystal in the QCM holder. The gold circular ring in (a) around the quartz crystal is one of the electrodes. The gray mark at picture (b) is an indicator for orientation.

3.3.1 The used samples

As mentioned in section 3.1.1.3, the used crystals were SC-cut (stress compensated) quartz crystals with gold electrodes. These quartz crystals are disc shaped with a diameter of 14 mm. They oscillate in thickness shear mode, with a fundamental resonance frequency of about 6 MHz. For the D_2^+ measurements, an iron-tungsten alloy called FeW (98.5 at% iron and 1.5 at% tungsten) was magnetron-sputter-deposited at IPP Garching, with a thickness of about 300 nm. As mentioned before it is a model system for the EUROFER steel [5], which can be of use as first wall material in recessed areas in future fusion devices.

For the Ar^+ measurements, pure iron was magnetron-sputter-deposited at the IPP Garching on polished quartz crystals. The thickness of these layers is about 400 nm. Furthermore, these quartz substrates have been polished in order to achieve a very smooth and shiny surface, whereas the unpolished samples are opaque.

In figures 3.5 a photograph of an unpolished sample can be seen. Figure 3.5 (a) is the quartz crystal disk with magnetron sputter deposited FeW layers. Figure 3.5 (b) shows the quartz crystal in the QCM holder.

3.3.2 The QCM measurement device

The QCM measurement device, seen in figure 3.6, is separated into two parts.

- The Faraday Cup (FC), seen in figure 3.6 (a), point ①.
- The QCM holder, seen in figure 3.6 (a), point ②.

In figure 3.6 (b) a cut through the whole device is shown. It shows the different parts of the FC and the QCM holder.

The Faraday Cup

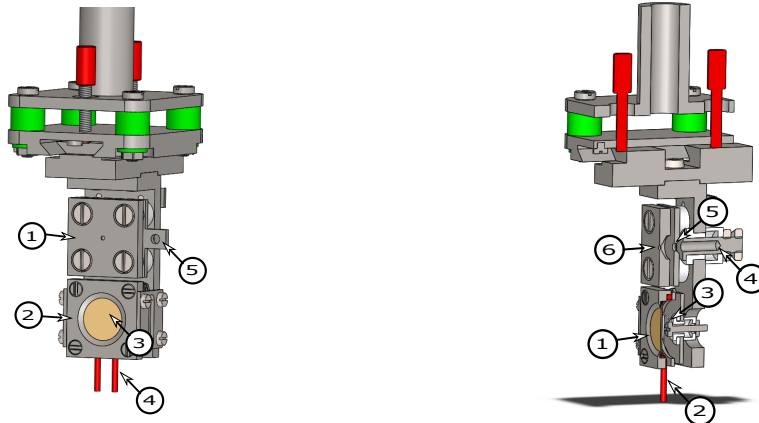
The Faraday Cup device features several parts. The main part is the FC chamber, seen in figure 3.6 (b), point ④. Here ions neutralize and the FC current is generated, which gives rise to the ion current. Due to ionization during ion impact with the wall in the FC chamber, secondary electrons can be emitted and eventually leave the FC chamber. This adds error currents to the measured FC current. Therefore, a so-called suppressor is applied, seen in figure 3.6 (b), point ⑤. This device consists of a plate with a small drill hole, where ions can enter the FC chamber. Furthermore, this plate is held on a negative potential of about -50 V , relative to the ground. This potential prevents electrons from escaping the FC chamber and ensures that no false currents appear. Lastly, there is the FC aperture, seen in figure 3.6 (b), point ⑥. Just like the suppressor this device also consists of a plate with a small hole through which ions can enter. The drill hole is of crucial importance in this case and must be precisely drilled since the drill hole size is the main parameter for ion current density measurements⁵. In this experiment the hole has an area of $A_{FC} = 0.97 \cdot 10^{-6}\text{ m}^2$ as evaluated from an optical microscope image.

The QCM holder

The main part of the QCM holder⁶ is the quartz crystal, seen in figure 3.6 (b), point ①. It is held in position by a tungsten spring, visible in figure 3.6 (b), point ③, which is also the electrical contact for the QCM electronics. Since every quartz crystal has a thermal minimum frequency (see chapter 3.1.1.3), the quartz needs a possibility for heating. This is assured by an ohmic heating wire, seen in figure 3.6 (b), point ②. Due to the holders design it is possible to achieve irradiation angles up to 70 degrees. At higher angles a shadowing effect due to some parts of the holder would occur.

⁵The importance of the drill hole is pointed out in section 3.3.5.

⁶This QCM holder (Version 2015) was designed by Bernhard M. Berger at the TU Wien.



(a) CAD drawing of the QCM measurement device.

- ① Faraday Cup
- ② QCM holder
- ③ QCM crystal
- ④ Heating wires for the QCM holder
- ⑤ Suppressor

(b) CAD cut view of the QCM measurement device.

- ① QCM crystal
- ② Heating wires for the QCM holder
- ③ Spring
- ④ Faraday Cup chamber
- ⑤ Suppressor drill
- ⑥ Faraday Cup aperture drill

Figure 3.6: CAD drawing of the QCM measurement device.

3.3.3 Setting up the setup

Before the setup can be used for measuring, a few steps have to be completed. After closing the vacuum vessel, the so-called "baking" has to be performed. Here the vacuum vessel is heated up to 430 K . This ensures that most of the water in the vacuum vessel is vaporised and pumped out. Usually, a baking time of at least 36 hours is necessary. Without this baking it would take too long to get rid of residual water molecules in the vacuum chamber. In section 3.1.1.1 the importance of having as little residual gases as possible in the vacuum chamber is pointed out.

3.3.4 Measuring procedure

A measuring cycle usually consists of several high fluence measurements/steps, where high fluences are applied to the samples under a specific angle of incidence. Afterwards a computer program calculates e.g. the sputter yield over fluence or other desired quantities, which then can be plotted. Between the high fluence steps short time measurements under different angles of incidence are usually performed.

Here the angle dependency of the sputter yield over a multitude of angles is measured, to see if the impact angle dependent sputter yield changes with increasing fluence. In some cases, AFM investigations are done, to investigate the surface behavior during irradiation.

In order to measure/calculate the mass removal rate/sputter yield with the QCM technique several essential measurements/adjustments have to be done:

- Adjusting the deflection plates and maximizing the ion current
- Measuring the ion current density
- Measuring the QCM resonance frequency over time during ion bombardment.

Adjusting the deflection plates and maximizing the ion current

First, the FC has to be placed in front of the ion source via the $xyz\phi$ -stage, so that the neutral beam is 9 *mm* off the FC center, to get rid of the neutral beam coming from the ion source. Afterwards, the ion source is activated with the desired acceleration voltage. Now the deflection plates (beam optics) are adjusted to bend the ion beam into the FC center. By altering the working gas pressure, tuning the ion gun and changing the deflection plate voltages, the beam can be fine tuned to maximize the ion current. In order to irradiate the probe homogeneously, the ion beam can be scanned over a large area by applying a scanning voltage (zig-zag shaped) to the deflection plates, or by intentionally defocussing the ion beam. The defocussing of the ion beam is achieved via the ion gun internal Einzel-lens.

Ion current density

The maximized, adjusted and scanned/defocused ion beam is checked by moving the FC in steps of 1 *mm* in both transverse directions of the ion beam, ± 4 *mm*. Variations in the current density should be kept below 5% to achieve a constant and homogeneous irradiation cycle and subsequently a homogeneous sputter process on the quartz sample. Otherwise, adjusting the ion beam needs to be repeated. With this information the ion current density can be calculated via the formula:

$$Q[C/m^2] = \int I(t)dt/A_{FC}. \quad (3.3)$$

Here $I(t)$ correspond to the measured ion current and A_{FC} is the FC drill hole area.

The ion current for the D_2^+ measurements varied between 60 and 70 nA , which corresponds to an ion flux of about $10^{17} \text{ ions } s^{-1} m^{-2}$. For the Ar^+ measurements the ion current varies between 6-7 nA , which corresponds to an ion flux of $10^{16} \text{ ions } s^{-1} m^{-2}$.

Due to the design of the QCM measurement device, it is not possible to do ion current measurements while measuring with the QCM. But it is possible to measure the relative ion current change via the additional aperture, mentioned in section 3.2 during measuring with the QCM.

Measuring the QCM resonance frequency over time

After finishing the ion current density measurements, the ion gun acceleration voltage is switched off and the QCM with the sample is placed in the ion beam exactly where the FC was previously. Now the resonance frequency of the quartz crystal sample over time can be logged. Before starting the ion bombardment, a so-called "beam-off" phase is recorded to ensure the sample does not undergo temperature drifts or unstable jumps in frequency. After a sufficiently long beam-off phase (50-100 seconds), the acceleration voltage is switched on again. Now the actual measurement starts. Meanwhile, the sample's resonance frequency is still logged. Typically a measurement takes 800 seconds to 70 ks , depending whether it is a short time measurement or a high fluence measurement. To finish the measurement, the acceleration voltage of the ion gun is switched off again. This is followed by another beam-off phase while the resonance frequency is still logging. This ensures that drift effects, etc. on the quartz can be seen. After the beam-off phase another ion current density measurement is done to check if the ion current varied during the measurements and to estimate errors. In figure 3.7 an actual measurement can be seen. In the first 50 seconds the beam-off phase can be seen. At time stamp $t=50 \text{ s}$ the actual measurement starts and lasts until $t=750 \text{ s}$. The red line from $t=500 \text{ s}$ to 750 s is the linear fit to the measured curve, which is used to calculate the sputter yield. From $t=750 \text{ s}$ to 800 s another beam-off phase is visible.

The insert at the lower right in figure 3.7 displays the calculated slope $\Delta f/\Delta t$ and the calculated sputter yield with its errors, according to the beam-off phase fits and ion current errors. The ion flux with its errors is also displayed.

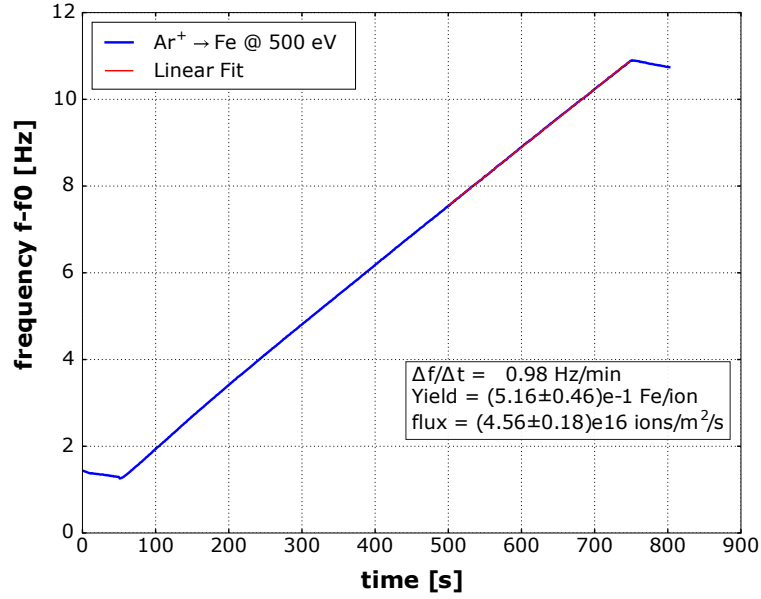


Figure 3.7: A frequency over time measurement, done with the modified setup. As projectile Ar^+ are used which sputter an iron surface. The impact angle is 0 degrees. The blue curve corresponds to the measured data. The red curve is a fit to the beam-on phase.

3.3.5 Calculating the sputter yield

According to the Sauerbrey equation 3.2, the relative mass loss $\Delta m/m$ is proportional to a relative change of the frequency $\Delta f/f$. For a quartz crystal, with a given resonance frequency f [Hz], a frequency change Δf , a thickness d_{quartz} , an area A_{quartz} and a density ρ_{quartz} , the relative mass removal Δm can be calculated via equation 3.2 [26].

$$\Delta m[kg] = -\rho_{quartz}d_{quartz}A_{quartz} \cdot \frac{\Delta f}{f} \quad (3.4)$$

In order to get rid of the actual surface area on the right hand side of the equation, equation 3.4 can be divided by A_{quartz} . Then the dimension of equation 3.4 reads $\Delta m[kg/m^2]$.

For the actual mass removal rate it is necessary to integrate the ion current over time per unit area to subsequently acquire the total charge per unit area and also the total number of impacting ions:

$$Q[C/m^2] = \int I(t)dt/A_{FC} \rightarrow Ions[1/m^2] = \int I(t)dt \frac{1}{A_{FC}e_0q} \quad (3.5)$$

with A_{FC} being the Faraday Cup pinhole aperture area, q the charge of the impacting ions and e_0 the elementary charge.

The average mass removal per incident ion then reads [26]:

$$y[kg/ion] = \frac{\rho_{quartz}d_{quartz} \cdot (e_0qA_{FC})}{\int I(t)dt} \cdot \frac{\Delta f}{f} \quad (3.6)$$

The sputter yield Y and the mass removal rate are connected by:

$$Y[atoms/ion] = \frac{y[kg/ion]}{m_t[kg]} \quad (3.7)$$

with m_t being the target particle mass.

For composite materials it is common to use the mass removal rate instead of the sputter yield. The sputter yield [atoms/ion] and the mass removal rate [amu/ion] are connected with each other over a constant factor, which depends on the mass of the components and the composition.

Experimental results

4.1 $D_2^+ \rightarrow FeW$

In this measurement series, the influence of surface enrichment of high-Z elements - in this case tungsten- due to preferential sputtering is investigated on FeW films with (98.5 at% iron and 1.5 at% tungsten). Furthermore, Atomic Force Microscope (AFM) investigations have been carried out in order to examine the surface structures before and after irradiation with deuterium fluences. All conducted measurements have been done under an extraction voltage of 500 V with D_2^+ molecules. Due to the fact that the binding energy of D_2 is low compared to its kinetic energy of 500 eV, D_2 molecules can be regarded as two separated D atoms, each of which has a kinetic energy of 250 eV. Three samples in total have been irradiated under different angles of incidence. The used samples featured a high initial roughness, as seen in figure 4.3 (a). The total fluence used for each sample was $\sim 3.3 \cdot 10^{23} D/m^2$.

4.1.1 High fluence measurements

The three conducted measurement series were done at irradiation angles $\alpha = 0, 45$ and 60 degrees, measured from the surface normal. The experimental results under normal angle of incidence ($\alpha = 0$ degrees) are displayed in figure 4.1(a). Initially, for small fluences, the mass removal rate of the FeW samples is comparable to the results of pure iron samples (green curve). With increasing fluence the mass removal rate of the FeW samples deviates from the pure iron sample. The observed reduction of the mass removal rate, which is due to preferential sputtering of iron and the surface enrichment of tungsten, is in agreement with results shown in [28, 29]. The data from the fifth measurement in figure 4.1(c) is off the expected position, probably because of bad connections and/or a failure in the ion gun.

After this incident the further measurements did not behave as expected. Therefore, the measurement series in figure 4.1(c) is only plotted until the incident with a fluence of $\sim 1.5 \cdot 10^{23} D/m^2$. It was not possible to investigate the setup at this point to prove the assumptions. Nonetheless, the qualitative behavior of a linear decrease of the mass removal rate with increasing fluence can be seen. The small gaps between each measurement are due to cut-offs at the beginning of plotting, for better visibility. Furthermore, before each measurement several small fluences have been applied for the angle dependent measurements, see next section.

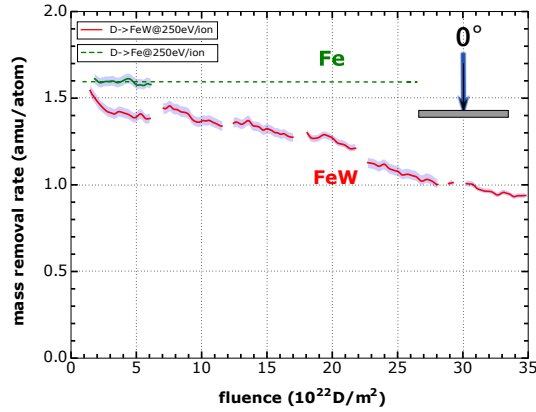
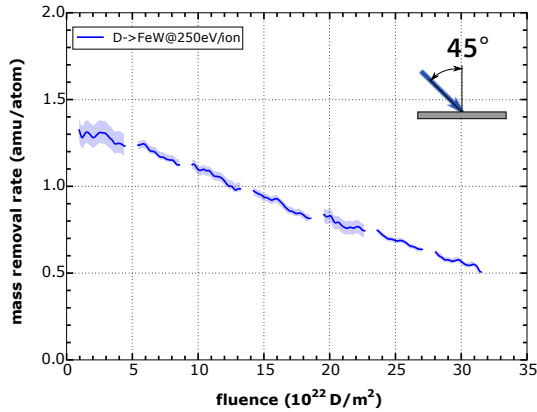
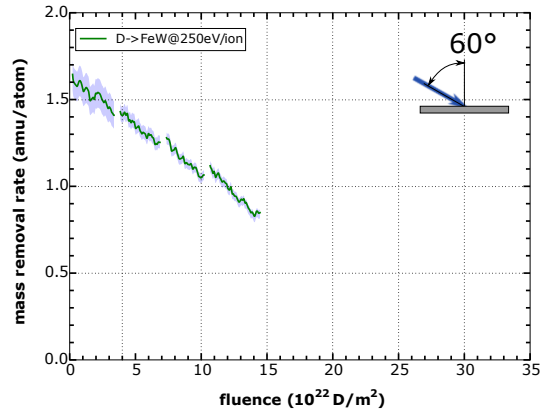
(a) High fluence irradiation under **0 degrees**(b) High fluence irradiation under **45 degrees**(c) High fluence irradiation under **60 degrees**

Figure 4.1: All high fluence measurements of the FeW samples. In all measurements (a), (b) and (c) a decrease of the mass removal rate with increasing fluence is visible. The green curve in (a) corresponds to a pure iron sample.

4.1.2 Short time angle dependent measurements

As mentioned before, each long term irradiation cycle is followed by a short time interval in which the angular dependent sputtering yields were measured to see whether there is a fluence dependence of the sputtering yield versus surface angle. Such a behavior can indeed be seen in figures 4.2(a)-(c) before irradiation and after applying a total deuterium fluence of $\sim 3.3 \cdot 10^{23} D/m^2$. These figures show how the angular dependence changes with increasing fluence as already observed in figures 4.1(a)-(c). In figures 4.2(a) ($\alpha = 0$) the angle dependency stays qualitatively the same over high fluences. A different situation occurs in figure 4.2(c) ($\alpha = 60$) and 4.2(b) ($\alpha = 45$) in which the behavior before irradiation and after applying high fluences differs when using higher angles.

In figure 4.3 the corresponding AFM images of the samples before and after irradiation can be seen. Figure 4.3(a) shows a non-irradiated FeW sample. It displays a grain-like structure with a grain length of typically 200 nm and a grain height of 10-15 nm. A root mean square roughness of typically 3.2 nm can be derived from the AFM measurement (see table 4.1). For the irradiated sample under 60 degrees (figure 4.3(d)) ripple formation is visible. In this case Perpendicular Mode Ripple (PeMR) [16]. The grain length is approximately the same compared to the non-irradiated sample but the grain height and the root mean square roughness is nearly tripled, as can be seen in table 4.1. In figures 4.3 (b) and (c) the root mean square roughness and the grain height are doubled compared to the non-irradiated sample but the grain length is reduced. In 4.3(b) a dot-like structure forms while the grain-like structure completely vanishes. In 4.3(c) the beginning of the same ripple formation as in 4.3(d) is visible.

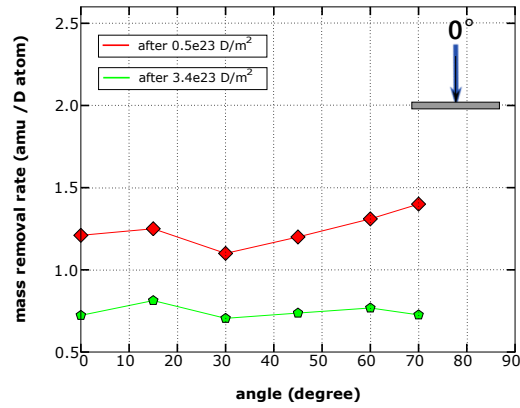
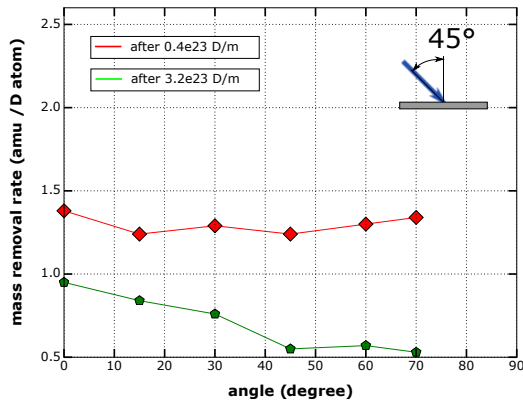
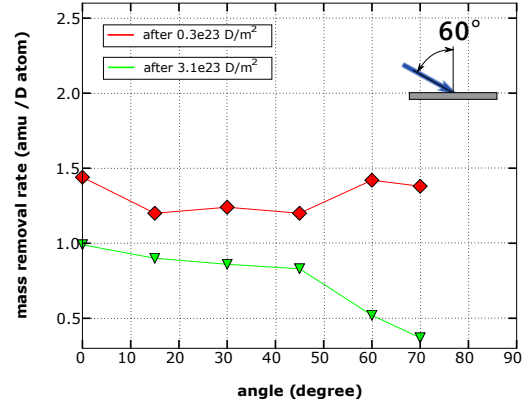
(a) Angle-dependent plot under **0 degrees**(b) Angle-dependent plot under **45 degrees**(c) Angle-dependent plot under **60 degrees**

Figure 4.2: These figures display ion impact angle dependent measurements for D^+ on FeW, done in between high fluence measurements. Just as in figures 4.1 the angle mass removal rate decreases with increasing fluence of all impacted angles.

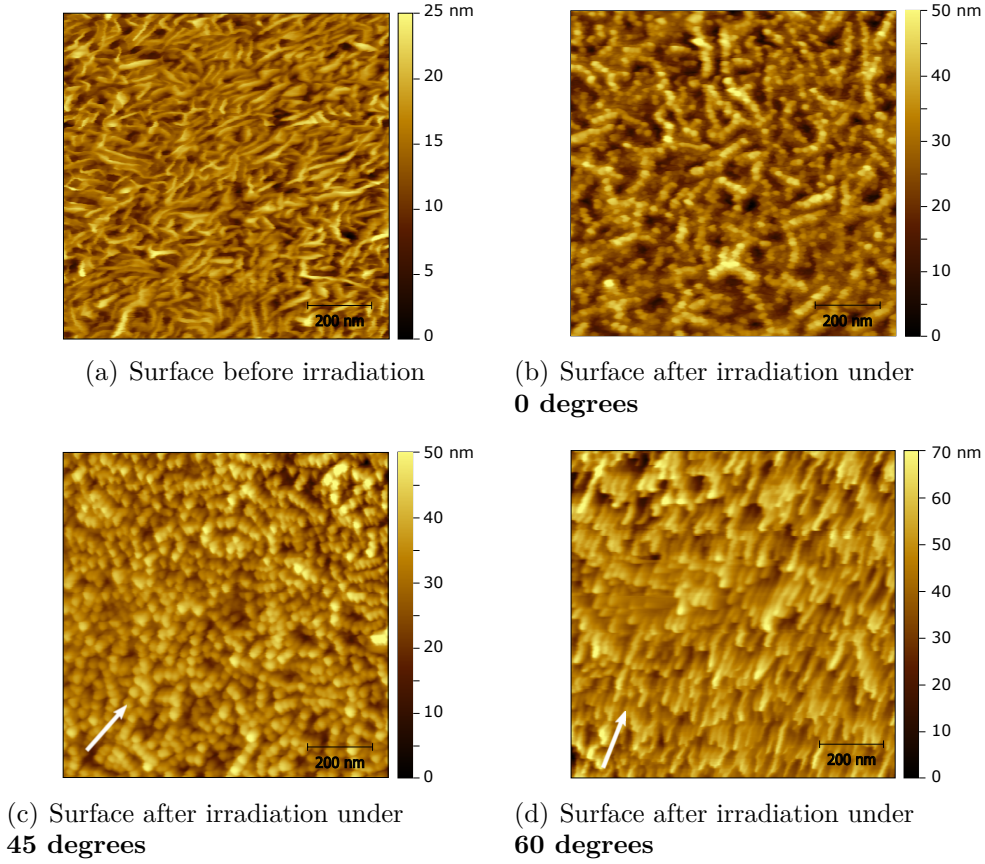


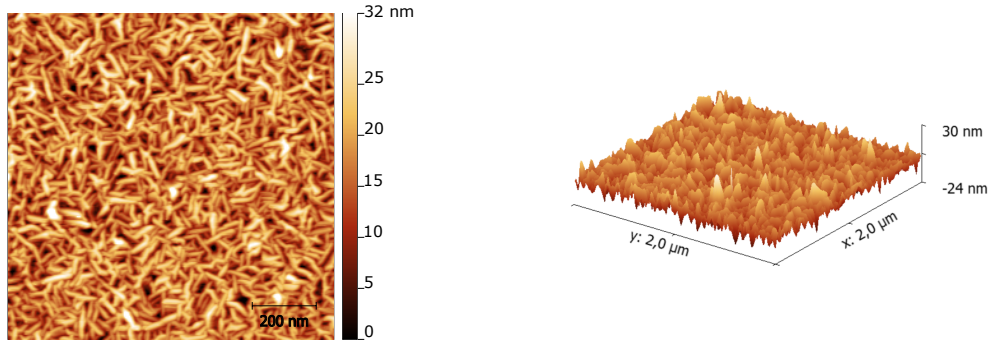
Figure 4.3: This figure shows the surfaces of the samples before (a) and after (b)-(d) irradiation with $250 \text{ eV}/D$ deuterium fluences after certain fluences. The samples were irradiated under **0** (b), **45** (c) and **60** (d) **degrees** and the applied fluence was $\sim 3.3 \cdot 10^{23} D/m^2$. The white arrows indicate the direction of irradiation. In (c) and (d) signs of pattern formation are visible, whereas in (a) no and in (b) only little signs occur. In (b) a dot-like structure and in (c) the beginning of pattern formation can be seen. The figures are taken from reference [31].

	virgin sample	$\alpha = 0^\circ$	$\alpha = 45^\circ$	$\alpha = 60^\circ$
RMS	3.2 nm	8.6 nm	6.4 nm	10.5 nm

Table 4.1: Root mean square roughness (RMS) of the AFM images in figure 4.3.

4.2 $Ar^+ \rightarrow Fe$

In this measurement series the fluence dependency of surface structure formations, such as ripples, are investigated on a pure iron film. In order to have clean sputter conditions, effects like preferential sputtering and initial rough surfaces, which could compromise the appearance of ripples, must be suppressed. Therefore, the used samples are polished and coated with pure iron. In figure 4.4 such an unirradiated sample can be seen in an AFM picture. The root mean square roughness RMS value is $\sim 5.19 \text{ nm}$. Instead of deuterium, argon ions were used. This is due to a better QCM signal with argon, since argon implies a much higher sputter yield on iron than deuterium. Furthermore, due to the high sputter yield of argon the influence of the residual gas ions, which can also be accelerated towards the target and work as a sputtering agent, is much smaller than it would be with deuterium.



(a) AFM image of a non-irradiated iron quartz sample. (b) 3D Plot of the non-irradiated sample.

Figure 4.4

All measurements have been conducted under an extraction voltage of 500 V with Ar^+ ions. In total, four samples have been irradiated under different angles of incidence. The total fluence for each sample was $\sim 6.8 \cdot 10^{21} \text{ Ar}/\text{m}^2$.

There have been two measurement series at irradiation angles $\alpha = 45$ and 60 degrees. Each series consisted of two parts:

- A high fluence measurement with the QCM under an irradiation angle α . Angle dependent sputter yield measurements were conducted before and after high fluence irradiation of the sample, in order to investigate the fluence dependency of the angle dependent sputter yield. These measurements -high fluence and angle-dependent- had two main goals: Firstly to monitor fluence dependent evolution of the sputter yield and secondly to investigate if the initial surface roughness of the samples influences the angle-dependent sputter yield.

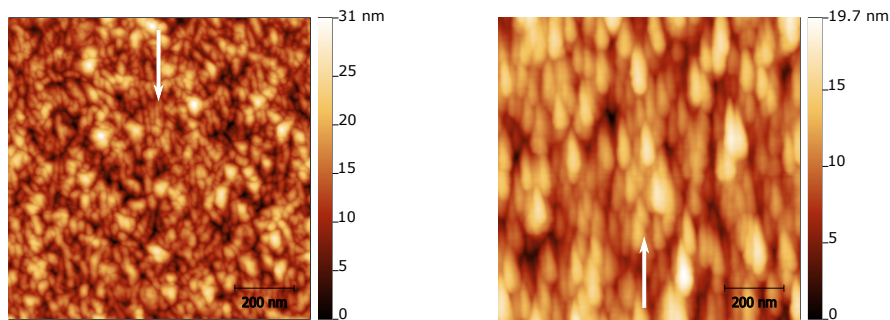
- Measurements, in which the sample surface was irradiated in fluence steps, under a defined angle. This was achieved via the additional aperture mentioned in section 3.2. In total, four steps per measurement cycle were conducted. This allows the investigation of the evolution of the surface structure after every fluence step.

In the following sections the results of the different measurement cycles will be displayed.

4.2.1 High fluence measurements

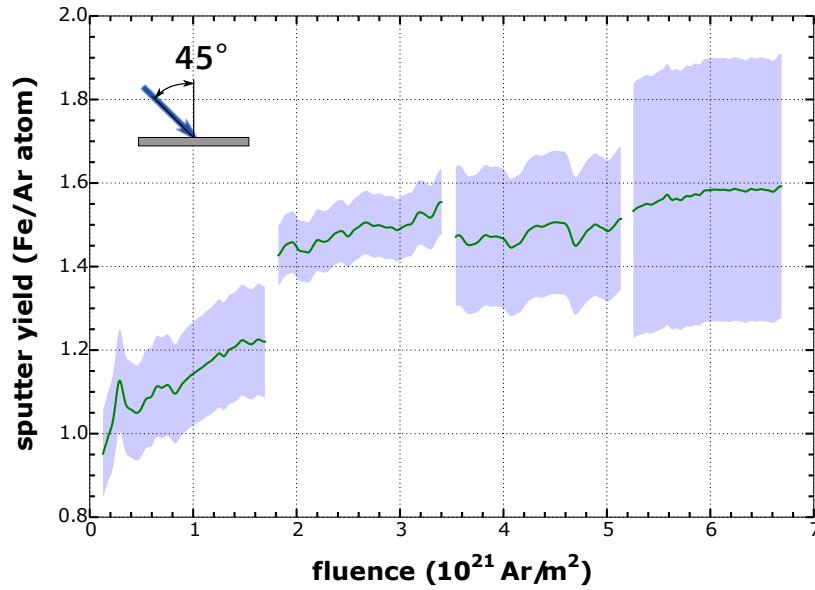
The two conducted measurement series were done at irradiation angles $\alpha = 45$ and 60 degrees with iron-coated quartz crystals. Firstly, the sputter yield over fluence was measured with the QCM technique in four fluence steps up to $\sim 1.7 \cdot 10^{21} \text{ Ar}/m^2$. In total a fluence of $\sim 6.7 \cdot 10^{21} \text{ Ar}/m^2$ was applied to each sample. In figure 4.6 (a) and (b) the mass removal rate over fluence is displayed. Figure 4.6(a) displays the measurement under $\alpha = 45$ degrees and figure 4.6(b) the measurement under $\alpha = 60$ degrees. In both measurement series it is clear to see that the sputter yield starts at a minimum and achieves a steady state case at a fluence of $\sim 4 \cdot 10^{21} \text{ Ar}/m^2$. Due to instabilities of the ion gun during measurements, the sputter yield unfortunately features jumps and discontinuities. Especially in figure 4.6(b) it is easy to see at fluences in the area of $3.3 \cdot 10^{21} \text{ Ar}/m^2$ and $6.1 \cdot 10^{21} \text{ Ar}/m^2$.

Following the sputter yield measurements, AFM investigation were conducted [30] in order to identify surface modification on the samples after irradiation. These AFM investigations can be seen in figure 4.5 (a) and (b). Figure 4.5(a) corresponds to the sample which was irradiated under $\alpha = 45$ degrees and figure 4.5(b) to the sample irradiated under $\alpha = 60$ degrees. Especially in figure 4.5(b) clear PeMR patterns are visible. For a profound discussion of these results, see section 4.3.

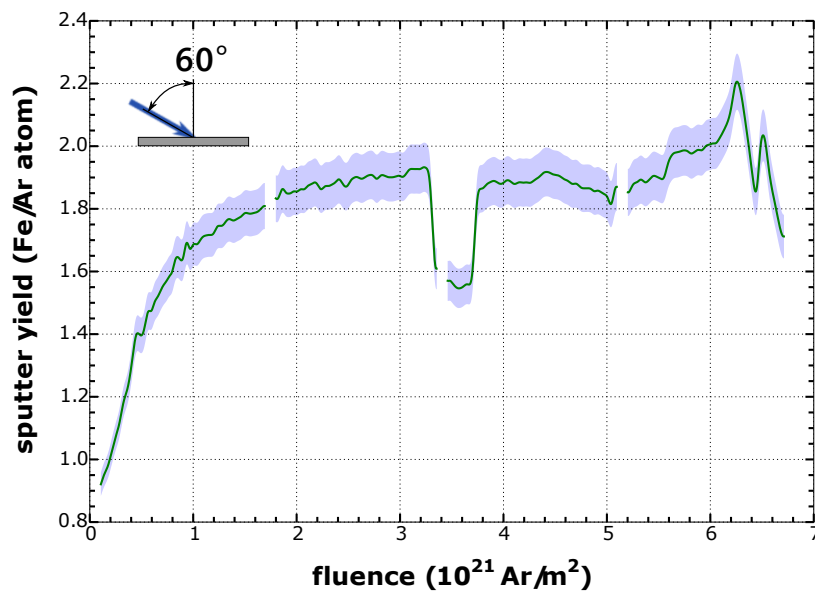


(a) The RMS value measures 4.18 nm. (b) The RMS value measures 3.79 nm.

Figure 4.5: AFM images of irradiated samples under 45 degrees, (a) and 60 degrees, (b). The white arrows indicates the direction of irradiation.



(a) Sputter yield plotted versus fluence for an irradiation of iron with 250 eV/D deuterium projectiles under an angle of 45 degrees. The total applied fluence is $\sim 6.7 \cdot 10^{21} \text{ Ar/m}^2$. The sputter yield reaches a steady state case of approximately 1.45 Fe/Ar at a fluence of $\sim 4 \cdot 10^{21} \text{ Ar/m}^2$.



(b) Sputter yield plotted versus fluence for an irradiation of iron with 250 eV/D deuterium projectiles under an angle of 60 degrees. The total applied fluence is $\sim 6.7 \cdot 10^{21} \text{ Ar/m}^2$. The sputter yield reaches a steady state case of approximately 1.83 Fe/Ar at a fluence of $\sim 4 \cdot 10^{21} \text{ Ar/m}^2$.

Figure 4.6

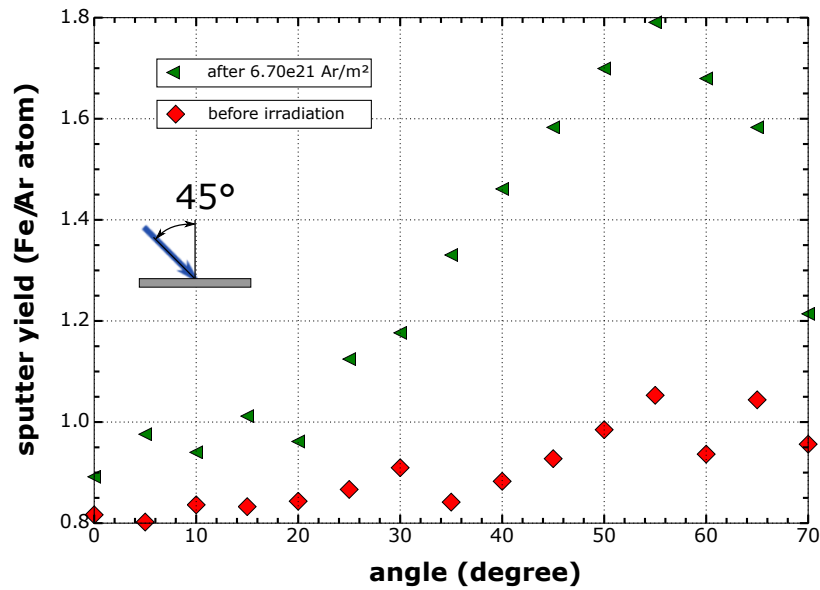
4.2.2 Angle-dependent measurements

Before and after each measurement series, angle dependent measurements have been conducted. Here the angle dependency of the sputter yield over a large variety of angles has been measured. The results of these measurements can be seen in figures 4.7(a) and (b). Figure 4.7(a) corresponds to the sample irradiated under $\alpha = 45$ degrees and figure 4.7(b) corresponds to the sample irradiated under $\alpha = 60$ degrees. In both measurements clear differences between before and after irradiation can be seen. While before irradiation no significant angle dependency can be determined, after irradiation a clear dependency is visible. For a profound discussion, see section 4.3.

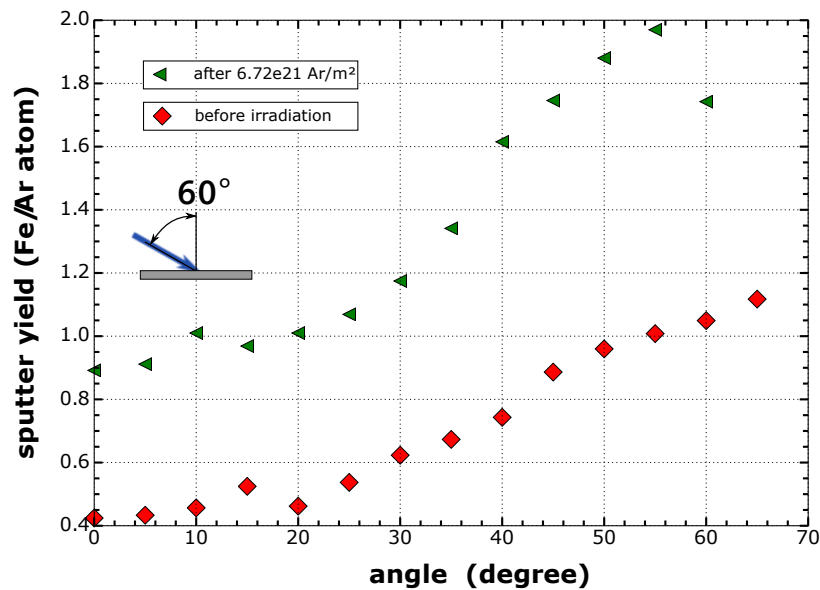
4.2.3 Fluence step measurements with aperture

In order to investigate the fluence-dependent formation of surface structures an additional irradiation with iron-coated silicon plates has been conducted. In total two additional measurement series were carried out. One at $\alpha = 45$ degrees and one at $\alpha = 60$ degrees. Here the same four fluence steps each up to $\sim 1.7 \cdot 10^{21} Ar/m^2$ like in the high fluence case were applied to each sample. This time the additional aperture was used to shade parts of the sample so that different fluence steps could be used. The first step had a fluence of $\sim 1.7 \cdot 10^{21} Ar/m^2$, the second $\sim 3.4 \cdot 10^{21} Ar/m^2$, etc.. After irradiation the samples were investigated with an AFM [30]. Here every fluence step was separately evaluated. The results can be seen in figures 4.8(a)-(e) for the sample irradiated under $\alpha = 45$ degrees and figures 4.9(a)-(e) for the sample irradiated under $\alpha = 60$. RMS values corresponding to each AFM image are shown in the tables 4.2 and 4.3 below the figures.

After each step the formation of patterns becomes clearer. The surface changes from a grain/dot-like structure to a more "periodic" structure, the ripples. In case of the $\alpha = 45$ degrees measurement the RMS values increase with higher fluences, whereas in case of the $\alpha = 60$ degrees measurement the RMS values fall with higher fluences. In the end they are more or less comparable to each other. For a profound discussion of the results see section 4.3.



(a) Angle dependent sputter yield. Before irradiation (red square) and after irradiation (green triangle) with a fluence of $\sim 6.70 \cdot 10^{21} \text{ Ar}/m^2$ under 45 degrees.



(b) Angle dependent sputter yield. Before irradiation (red square) and after irradiation (green triangle) with a fluence of $\sim 6.72 \cdot 10^{21} \text{ Ar}/m^2$ under 60 degrees.

Figure 4.7

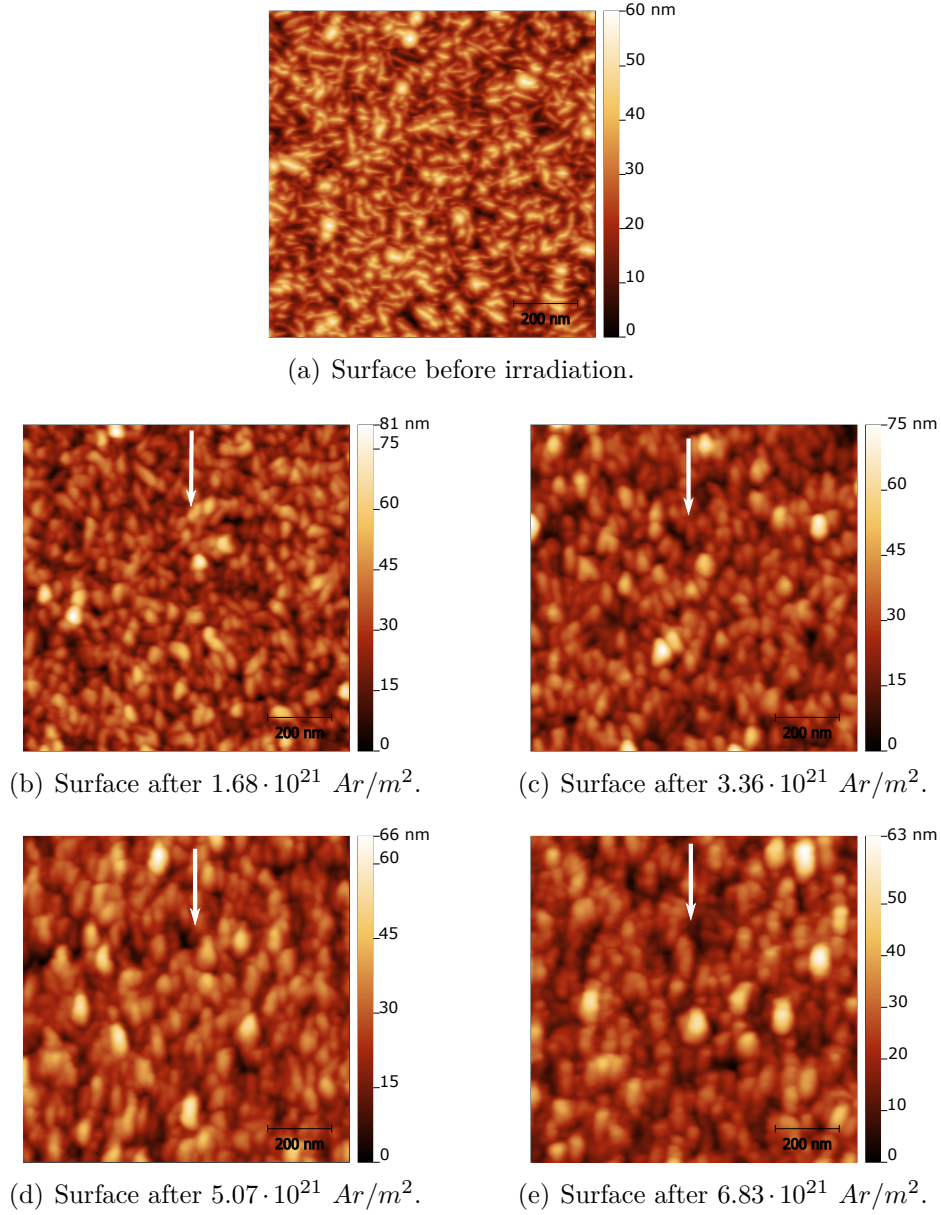


Figure 4.8: These figures show the surface of the iron samples before (a) and after (b)-(e) irradiation by $500 \text{ eV}/Ar$ under **45 degrees**. After each step the appearance of ripples becomes clearer. The white arrow indicates the direction of irradiation.

fluence [$10^{21} \text{ Ar}/m^2$]	virgin sample	1.68	3.36	5.07	6.83
RMS	7.76 nm	7.82 nm	9.16 nm	8.61 nm	9.29 nm

Table 4.2: Root mean square roughness (RMS) of the AFM images seen in figure 4.8.

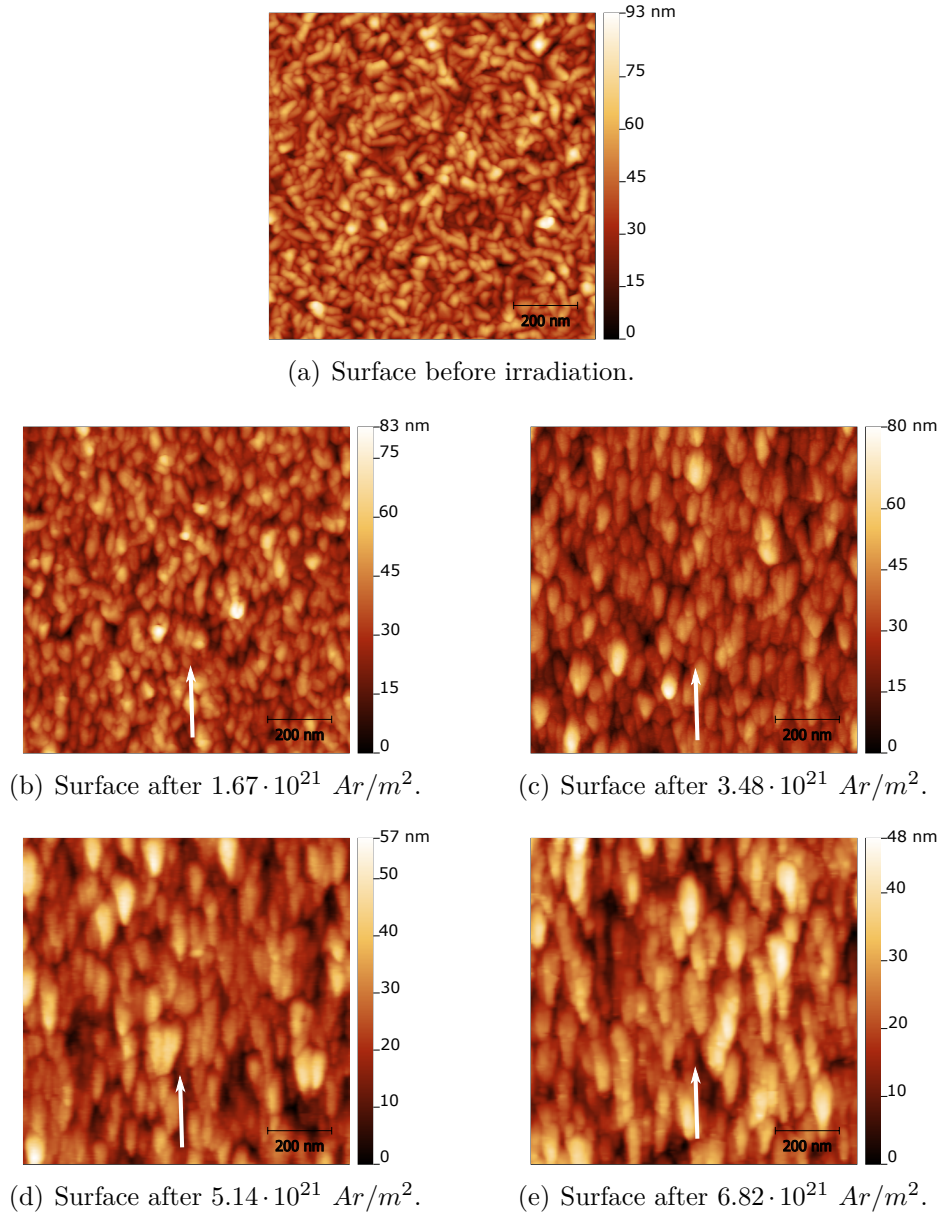


Figure 4.9: These figures shows the surface of the iron samples before (a) and after (b)-(e) irradiation $500 eV/Ar$ under **60 degrees**. After each step the appearance of ripples becomes clearer. The white arrow indicates the direction of irradiation.

fluence [$10^{21} Ar/m^2$]	virgin sample	1.67	3.48	5.14	6.82
RMS	10.1 nm	9.45 nm	8.42 nm	8.20 nm	8.30 nm

Table 4.3: Root mean square roughness (RMS) of the AFM images in figure 4.8.

4.3 Discussion

FeW samples

The behavior of the mass removal rate of FeW (98.5 *at%* iron and 1.5 *at%* tungsten) surfaces under deuterium fluences showed that the mass removal rate decreases with increasing fluence, as can be seen in figure 4.1. This is in agreement with observations reported in literature, see [28, 29, 31] and was attributed to preferential sputtering of iron and consequently an enrichment of the tungsten concentration.

The change in the mass removal rate over the change in fluence ($-\Delta m_{rr}/\Delta f_{lc}$) is also fluence-dependent, which is shown in figure 4.10. During initial irradiation stages (figure 4.10 a) the change in mass removal over change in fluence is different for each measurement series. In fact the $\alpha = 0$ degrees measurement series shows the the lowest $-\Delta m_{rr}/\Delta f_{lc}$, whereas the $\alpha = 60$ degrees measurements the highest $-\Delta m_{rr}/\Delta f_{lc}$. However, after a fluence of $\sim 3.3 \cdot 10^{23} D/m^2$ (figure 4.10 insert b) the values of all measurement series matches almost entirely.

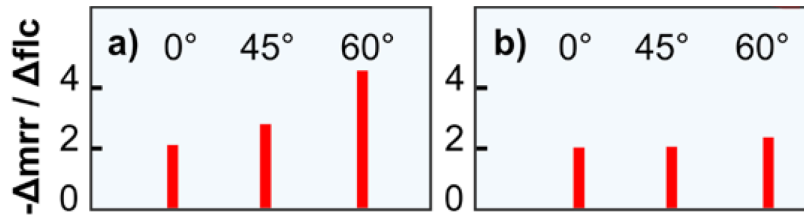


Figure 4.10: Change of the mass removal with fluence, for the three measurement series. a) displays the situation in the initial stages of irradiation and b) after $3.3 \cdot 10^{23} D/m^2$. Image from reference [31].

This behavior can be well understood. The Bradley-Harper theory states that the mass removal rate is highly dependent on the angle of incidence, see section 2.2.1. Irradiation under higher angle of incidence usually leads to a higher mass removal rate.

On the other hand the effects of preferential sputtering of iron in the FeW surface layers takes its toll. The increase of the iron sputtering yield with impact angle due to preferential sputtering, accelerates the development of a tungsten-enriched surface. High tungsten concentrations in the surface-near region in turn reduce the sputter yield with increasing fluence, because tungsten is not as easily sputtered as iron. The surface also becomes rougher with higher fluences, see figures 4.3(a)-(d).

For rough surfaces however, the dependence of the sputtering yield on the ion impact angle is considerably reduced, since the yield has to be averaged over a distribution of impact angles. With this information the above mentioned behavior of the change in mass removal rate over fluence (seen in figure 4.10) can be explained. The surface roughening after irradiation of the samples can be seen in figure 4.3, as explained previously.

The samples used in this experiment initially have relatively broader angular distribution (simply put, a rough surface). Therefore, with the arguments from above, the measured mass removal rates are lower than would be expected due to e.g. computer simulations programs like SDTrimSP, which only consider completely flat surfaces. In figure 4.11 a SDTrimSP calculation is shown (green curve at $\sim 1 \cdot 10^{23} D/m^2$) compared to measurements at $\sim 1 \cdot 10^{23} D/m^2$. In order to improve the agreement between simulated data and measured data the SDTrimSP program would have to be modified, so that it could be run with initially rough surfaces. This way the simulations could very probably be improved.

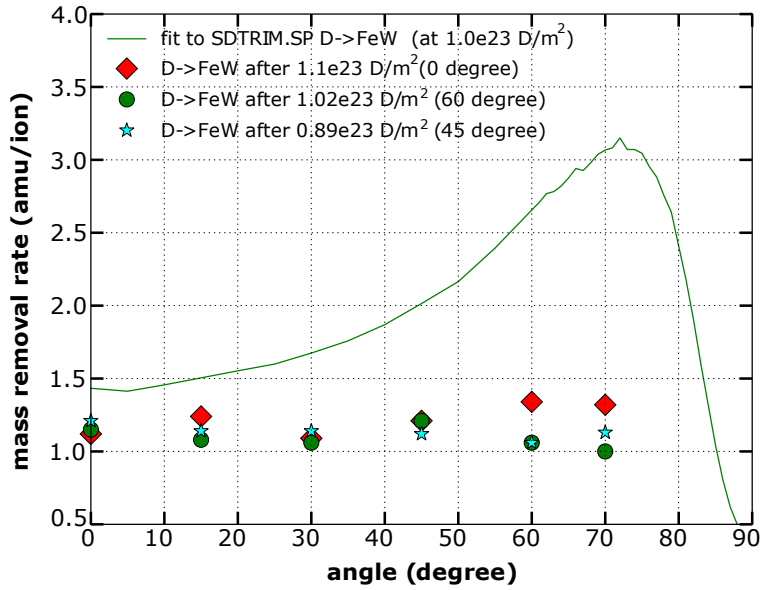


Figure 4.11: Plot of three angle dependent measurement series: \blacklozenge (0 degrees), \bullet (60 degrees) and \star (45 degrees). The green line shows results for a flat surface simulated by the SDTrimSP program.

Another interesting result is, that the angle dependency of the mass removal rate for different high fluence measurements is only indicated, see figures 4.2(a)-(c). This is most likely due to the already mentioned initial roughness of the used samples. Which results in an ion impact angle distribution and therefore an altered mass removal rate.

Whereas the qualitative behavior of the $\alpha = 0$ results (figure 4.2(a)) stayed the same before and after irradiation ($\sim 3 \cdot 10^{23} D/m^2$), the angle dependency of the $\alpha = 45$ and the $\alpha = 60$ degrees measurement deviated before and after irradiation (figure 4.2(b) and (c)). This is most likely the effect of ripple formations, in this case PeMR. This ripple formation can be seen in the AFM image 4.3(d). The knee in the $\alpha = 45$ and 60 degrees measurement at the angles 45 degrees (in figure 4.2(b)) and 60 degrees in (in figure 4.2(c)) can be a resulting effect of preferential sputtering and the subsequent building of a directed tungsten "shield". Since iron is easier sputtered than tungsten, the previously mentioned preferential sputtering leads to an increase of tungsten at the surface. Behind this tungsten surface atoms, iron atoms line up. If the ion beam hits the surface under an angle this line up of iron atoms behind tungsten atoms is also under the ion beam angle. At lower angles than the ion impact angle, ions could hit behind such a shielding and therefore sputter more iron, which would result in a higher mass removal. At a critical angle (the angle of high fluence irradiation), the ions would hit more tungsten atoms, which would then result in a lowered sputter yield.

The root mean square roughness nearly tripled compared to the unirradiated sample, see table 3.1. With the information above this can be explained. Due to the formation of ripples the roughness increased and therefore the angular distribution is broader. The impact angle for ions hence was an average over a large distribution of angles, which in turn reduced the overall mass removal rate. In the $\alpha = 0$ and 45 degrees measurements this effect is not as significant and therefore the effect on the mass removal rate is lower.

Fe samples

The high fluence measurements in figures 4.6(a) and (b) show a fluence dependency of the sputter yield. For pure iron samples the sputter yield should be nearly constant [14], but the trend follows an increasing sputter yield with increasing fluence. This effect is most likely due to an iron-oxide layer on the samples, which builds up during exposure to the atmosphere. The sputter yield of iron-oxide layers is much lower than the one of pure iron. Therefore, the measured sputter yield is initially lower until the oxide layers are sputtered. Another effect that could be involved in this behavior is the initial roughness -and therefore the angular distribution- of the surface of the samples. Since the sputter yield is dependent on the roughness of the sample (see previous sections) this can be an additional effect. In both samples the sputter yield achieves a steady state case at a fluence of $\sim 4 \cdot 10^{21} Ar/m^2$ (1.45 Fe/Ar in the $\alpha = 45$ degrees measurement and 1.83 Fe/Ar in the $\alpha = 60$ degrees measurement). The visible drop in the sputter yield in figure 4.6(b) at a fluence of $\sim 3.2 \cdot 10^{21} Ar/m^2$ to $\sim 3.8 \cdot 10^{21} Ar/m^2$ is most likely due to a drop in the ion current of $\sim 0.7 nA$. The unstable behavior of the sputter yield from $\sim 5.6 \cdot 10^{21} Ar/m^2$ is due to the ion current of the ion gun becoming unstable.

The fluence dependency of the angle dependent sputter yield in figures 4.7(a) and (b) shows that initially the sputter yield does not have a remarkable angular dependency. On the other hand, after the irradiation cycles both measurements series show a strong dependency of the measured sputter yield to irradiation angle. In figure 4.12 both results after the irradiation are displayed. As it is clear to see, both measurements fit nearly perfectly. The blue curve corresponds to a SDTrimSP calculation. Compared to the measurements, the qualitative behavior is remarkably accurate, although there is a certain off-set from the actual values.

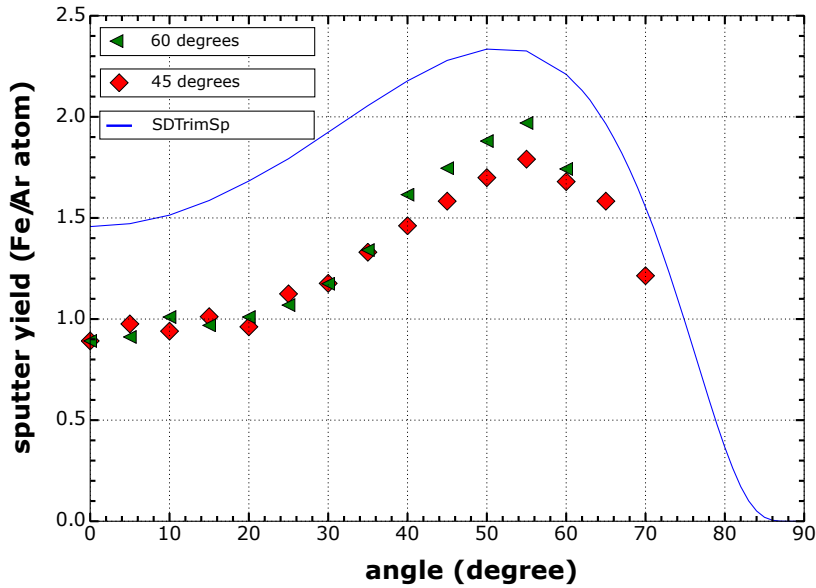


Figure 4.12: The angle dependency after irradiation of both Fe samples, compared to a SDTrimSP calculation. The green triangles \blacktriangleleft correspond to the $\alpha = 60$ degrees measurement and the red square \blacklozenge to the $\alpha = 45$ degrees measurement.

This means that after the same fluence both measurements irradiated under different angles of incident, show the same behavior in sputter yield and in angular dependency. The previous measurement results from the FeW samples do not show such behavior after irradiation. However, the RMS values of both FeW and polished Fe samples are comparable to each other, see tables 4.1, 4.2 and 4.3. This concludes that the RMS value is not a good quantity for measuring this kind of roughness and is not suitable for the role it has been given in the angle dependent sputter yield. In order to understand this situation, it is necessary to take a closer look at the definition of the RMS roughness value, which is:

$$R_{RMS} = \sqrt{\frac{1}{l} \int_0^l z^2(x) dx}. \quad (4.1)$$

Where l is the measuring length and $z(x)$ the profile values in the space of the measuring length l .

Equation 4.1 states, that only height modulations are taken into account. The angular distribution of the surface is completely neglected. In figure 4.13, schematics to clarify the situation are shown.

Both surfaces in figures 4.13 (a) and (b) are equivalent in the order of angular distributions. The RMS roughness values on the other hand are completely different -see inlays-. Therefore, the RMS roughness value can not be used in order to determine whether or not an angular dependency of the sputter yield is prevalent. The angular distribution of impact angles is a crucial part in the angle dependency of the sputter yield, as it was mentioned multiple times previously.

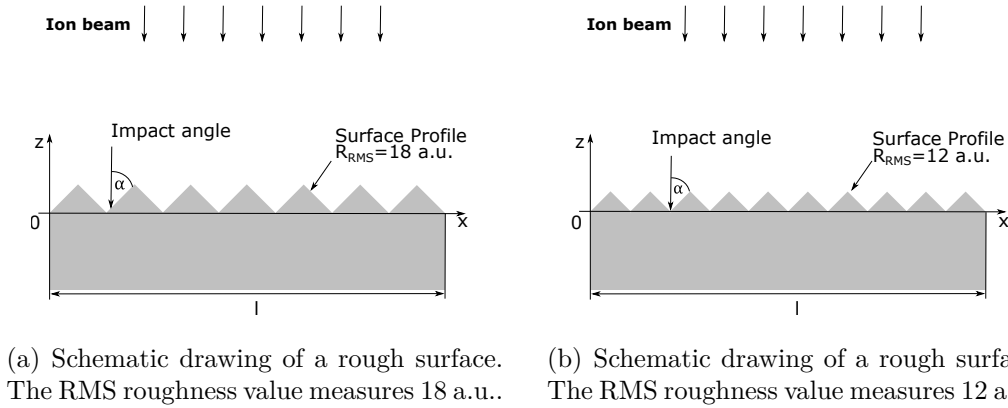
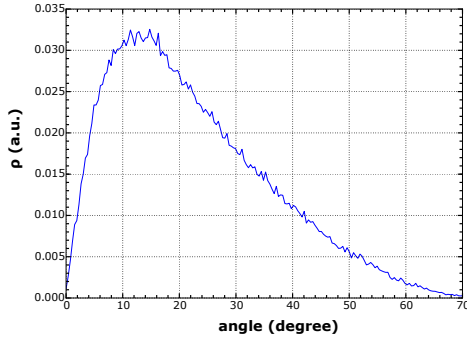


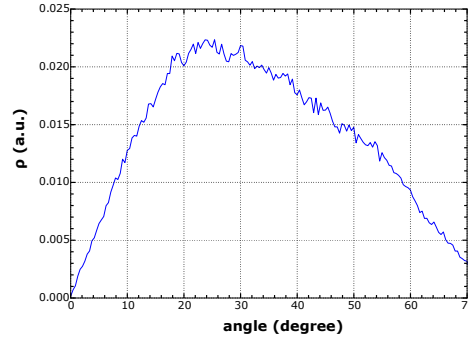
Figure 4.13: Schematics of a rougher (a) and a smoother surface (b). The impacting ions come from above and are perpendicular to the surface normal. In both images the local impact angles α are the same. Therefore, the angular distribution for both images should be equal. But the RMS roughness values are different.

In order to explain the occurrence of the angular dependency of the sputter yield on the polished Fe samples (see figures in 4.7) and why this dependency does not occur in the unpolished FeW samples (see figures in 4.2), it is necessary to take a closer look at the actual surfaces and their angle distribution. The angular distribution are obtained through an AFM investigation of the sample surface, like in figure 4.9. A computer program then is able to calculate the actual angle distribution. In figures 4.14(a)-(d) the angle distribution of surfaces from an Fe sample and an FeW sample are shown. It is clear to see that in both cases the angle distribution before irradiation is very broad. After irradiation the angle distribution of the surfaces clearly changes. In the case of the FeW sample (figures 4.14(a) and (b)) the angle distribution even got broader and the maximum of the distribution went towards higher angles.

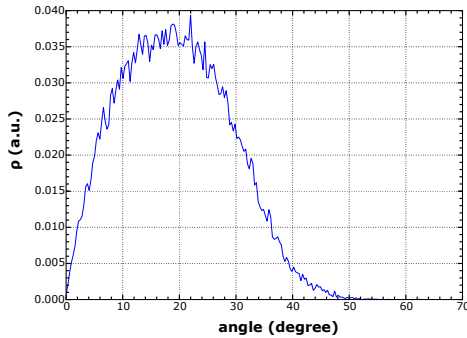
In the case of the Fe sample (figures 4.14(c) and (d)) the angle distribution got narrower and the maximum changed towards smaller angles. However, in the case of the FeW samples (figure 4.14(d)), the change is much more significant than in the FeW case (figure 4.14(b)). This shows that a narrow angle distribution is an indicator for an angle dependency of the sputter yield. In the Fe samples an angle dependency of the sputter yield was detected, which was not the case in the FeW samples.



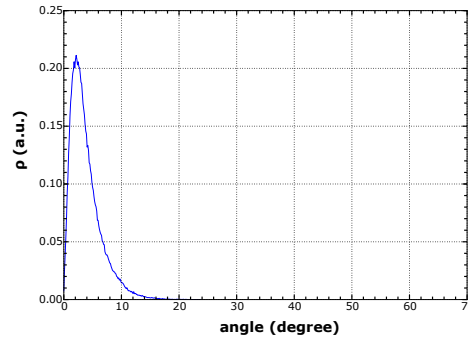
(a) FeW sample angle distribution before irradiation.



(b) FeW sample angle distribution after irradiation under **60 degrees**.



(c) Polished Fe sample angle distribution before irradiation.



(d) Polished Fe sample angle distribution after irradiation under **60 degrees**.

Figure 4.14: These figures show the angle distribution of FeW ((a) and (b)) and polished Fe ((c) and (d)) surfaces. (a) and (c) correspond to the situation before irradiation and (b) and (d) to the situation after irradiation under 60 degrees. Before irradiating the samples, a broad angular distribution is prevalent. After irradiating the unpolished FeW samples, angle distribution becomes even broader, whereas in the case of the polished Fe samples it becomes narrower.

This situation is in agreement with the results of computer simulations done by SDTrimSP. As it was mentioned before, this program currently only assumes completely flat surfaces, which means that the angular distribution of the used surfaces are Delta-functions.

Within this measurement series an angular dependency of the sputter yield was shown with narrow angle distributions and not with broad distributions. In order to cross-check this result, the simulations could be run again after modifying the SDTrimSP to include angle distributions within its code.

In figures 4.8(a)-(e) and 4.9(a)-(e) the AFM images corresponding to the fluence step measurements can be seen. After each fluence step the appearance of ripples -in this case PeMR- becomes stronger and stronger. In figure 4.8(a) the surface changes from a grain/dot-like structure to a more or less periodic ripple structure relatively fast (after $\sim 3.36 \cdot 10^{21} \text{ Ar}/m^2$). This behavior is even stronger in figure 4.9, in which the ripples are visible after the first fluence step of $\sim 1.67 \cdot 10^{21} \text{ Ar}/m^2$. In the end the ripple structure is extremely pronounced. An interesting result is, that the RMS values tend to decrease with increasing fluence in the $\alpha = 60$ degrees measurement, as can be seen in table 4.2. This could be explained by the ripple theory of Bradley-Harper, which predicts only an increase of the quasi-periodic modulations, which should result in higher RMS values.

Chapter 5

Conclusion

This work studied the influence of ion bombardment on FeW surfaces and polished Fe surfaces. Two main goals were pursued: Firstly, the surface enrichment of tungsten due to deuterium-ion bombardment on FeW alloy materials, to investigate its influence on the overall sputter yield under different angles of incidence. This was accomplished by using a QCM technique to measure the very small mass changes due to the ion bombardment. The second goal was to investigate the fluence and angle dependency of surface structures like ripples on pure Fe surfaces and compare them to changes in the sputtering yield with fluence. This was accomplished by investigating the samples at certain fluence steps after the irradiation using an AFM.

As a conclusion the surface enrichment of tungsten on FeW alloy materials is induced by so-called preferential sputtering. Here, one element is sputtered more easily than the other, resulting in an altered surface composition, which in turn changes the overall sputter yield. Due to the fact that in this experiment the kinetic energy of the projectile ions (250 eV/D) was at around the sputter threshold of tungsten, the effect of preferential sputtering was enhanced. The investigations showed the expected result, that the overall sputter yield decreased with increasing fluence. This is a direct indicator that on the surface a tungsten enrichment has taken place. Furthermore, no significant angle dependency of the sputter yield can be seen, be it before or after irradiation of the sample. AFM investigations on the samples showed, that due to the high initial roughness of the samples a broad angle distribution of the surface was prevalent. This broad angle distribution led to a large variety of impact angles during irradiation of the sample, which in turn reduced the angle dependency of the sputter yield significantly.

The fluence-dependent surface structure formation measurements on polished Fe surfaces clearly showed that at irradiation angles of 60 degrees the appearance of surface structures -in this case PeMR- build up very fast (after a fluence of $\sim 1.7 \cdot 10^{21} \text{ Ar/m}^2$), whereas under 45 degrees irradiation the appearance of ripples is significantly lower.

These experiments also showed a more pronounced angular dependency of the sputter yield after irradiation. This is due to a smoothening effect of the surface due to ion bombardment and therefore a narrower angle distribution on the surface. Furthermore, this experiment showed, that the used RMS roughness value is not a good quantity to determine whether or not an angular dependency of the sputter yield is prevalent, since most of the RMS values of the irradiated samples (Fe and FeW samples) were comparable to each other. Only by investigating the angle distribution of the surfaces a clear difference could be determined.

In order to cross-check the assumption with the angle dependency of the sputter yield and the angle distribution of the surfaces, computer simulations with e.g. SDTrimSP will have to be performed. Here, the program should assume a surface angle distribution similar to the ones in the measurements. Currently, the SDTrimSP program only assumes completely flat surfaces, which result in a Delta-function-shaped angle distribution.

The experiment proves the importance of these measurements, be it the processes of surface enrichment of e.g. high-Z elements in alloy materials like EUROFER during particle bombardment, which might be used in recessed areas in future fusion devices, as a cheaper and easy-to-use material. Or be it the understanding behind the angle dependency of the sputter yield on rough or smooth surfaces, which have an influence on the lifetime of plasma facing materials.

Bibliography

- [1] M. van der Hoeven. *World Energy Outlook 2013*. 2013.
- [2] Wikipedia. Chicago pile-1 — wikipedia, the free encyclopedia, 2016. [Online; accessed 2-November-2016].
- [3] K. Hans Wedepohl. The composition of the continental crust. *Geochimica et Cosmochimica Acta*, 59:1217–1232, 1995.
- [4] ITER.org. What kind of nuclear waste will be produced by iter, and in what quantity, 2016. [Online; accessed 2-November-2016].
- [5] R. Lindau, A. Moeslang, M. Rieth, M. Klimiankou, E. Materna-Morris, A. Alamo, A.-A. F. Tavassoli, C. Cayron, A.-M. Lancha, P. Fernandez, N. Baluc, R. Schaeublin, E. Diegele, G. Filacchioni, J.W. Rensman, B.v.d. Schaaf, E. Lucon, and W. Dietz. Present development status of {EUROFER} and ods-eurofer for application in blanket concepts. *Fusion Engineering and Design*, 75-79:989 – 996, 2005. Proceedings of the 23rd Symposium of Fusion TechnologySOFT 23.
- [6] H. A. Bethe and R. F. Bacher. Nuclear physics a. stationary states of nuclei. *Rev. Mod. Phys.*, 8:82–229, Apr 1936.
- [7] Wikipedia. Nuclear binding energy — wikipedia, the free encyclopedia, 2016. [Online; accessed 20-November-2016].
- [8] W. Demtröder. *Experimentalphysik 4 - Kern-, Teilchen- und Astrophysik*. Springer Spektrum, 2010.
- [9] D. R. Williams. NASA sunfact sheet, 2016. [Online; accessed 11-November-2016].
- [10] D.H. Perkins. *Particle Astrophysics*. Oxford Master Series in Condensed Matter Physics. Oxford University Press, 2003.
- [11] Max-Planck-Institut fuer Plasmaphysik. Fusionsanlagen, 2016, <http://www.ipp.mpg.de/9752/anlagentypen>. [Online; accessed 11-November-2016].

- [12] Max-Planck-Institut fuer Plasmaphysik. IPP Summer University for Plasma Physics Report, 2016.
- [13] W. Demtröder. Experimentalphysik 1 - Mechanik und Wärme. Springer Spektrum, 2008.
- [14] W. Eckstein. Physical sputtering and reflection processes in plasma-wall interactions. *Journal of Nuclear Materials*, 248:1–8, 1997.
- [15] R. Behrisch and W. Eckstein. Sputtering by Particle Bombardment I : experiments and computer calculations from threshold to MeV energies. 110, 2007, Springer Berlin Heidelberg.
- [16] T. Škeren, K. Temst, W. Vandervorst, and A. Vantomme. Ion-induced roughening and ripple formation on polycrystalline metallic films. *New Journal of Physics*, 15:1–20, 2013.
- [17] R. M. Bradley and J. M. E. Harper. Theory of ripple topography induced by ion bombardment. *Journal of Vacuum Science and Technology A*, 6:2390–2395, 1988.
- [18] P. Sigmund. Theory of sputtering. I. Sputtering Yield of Amorphous and Polycrystalline Targets. *Phys. Rev.*, 184:383–416, 1969.
- [19] J. Erlebacher, M. J. Aziz, E. Chason, M. B. Sinclair, and J. A. Floro. Spontaneous pattern formation on ion bombarded Si(001). *Phys. Rev. Lett.*, 82:2330–2333, 1999.
- [20] Y. Kuramoto and T. Tsuzuki. Persistent Propagation of Concentration Waves in Dissipative Media Far from Thermal Equilibrium. *Progress of Theoretical Physics*, 55:356–369, 1975.
- [21] G.I. Sivashinsky. Nonlinear analysis of hydrodynamic instability in laminar flames i. derivation of basic equations. *Acta Astronautica*, 4:1177 – 1206, 1977.
- [22] W. Eckstein A. Mutzke, R. Schneider and R. Dohmen. SDTrimSP version 5.00, IPP report, 12/8. 2011.
- [23] A. Mutzke and W. Eckstein. Ion fluence dependence of the Si sputtering yield by noble gas ion bombardment. *Nuclear Instruments and Methods in Physics Research Section B: Beam Interactions with Materials and Atoms*, 266:872 – 876, 2008.
- [24] K. Wittmaack. Rapid-relocation model for describing high-fluence retention of rare gases implanted in solids. *Nuclear Instruments and Methods in Physics Research Section B: Beam Interactions with Materials and Atoms*, 267:2846 – 2857, 2009.
- [25] N. Menzel and K. Wittmaack. Modification of stationary xenon implantation profiles in silicon by low-energy postbombardment with inert-gas ions. *Nuclear Instruments and Methods in Physics Research Section B: Beam Interactions with Materials and Atoms*, 7:366 – 370, 1985.

- [26] G. Hayderer, M. Schmid, P. Varga, HP. Winter, and F. Aumayr. A highly sensitive quartz-crystal microbalance for sputtering investigations in slow ion surface collisions. *Review of Scientific Instruments*, 70:3700, 1999.
- [27] G. Sauerbrey. Verwendung von Schwingquarzen zur Waegung duenner Schichten und zur Mikrowaegung. *Z. Phys.*, 155:206–222, 1959.
- [28] J. Roth, K. Sugiyama, V. Alimov, T. Höschen, M. Baldwin, and R. Doerner. EUROFER as wall material: Reduced sputtering yields due to W surface enrichment. *Journal of Nuclear Materials*, 454:1–6, 2014.
- [29] K. Sugiyama, J. Roth, V. Kh. Alimov, K. Schmid, M. Balden, S. Elgeti, F. Koch, T. Höschen, and Doerner R. P. Baldwin, M. J. Erosion study of Fe–W binary mixed layer prepared as model system for RAFM steel. *Journal of Nuclear Materials*, 463:272–275, 2014.
- [30] D. Mayr. Roughness-investigation of thin fe- and au layers under ar ion bombardment. *Project work TU Wien, 2016 unpublished*.
- [31] B. M. Berger, R. Stadlmayr, D. Blöch, E. Gruber, K. Sugiyama, T. Schwarzslinger, and F. Aumayr. Erosion of fe-w model systems under normal an oblige d ion irradiation. *Submittet for publication to Numerical Methods in Engineering*.

Danksagung

Zu allererst möchte ich mich bei meinen Eltern für ihre langjährige Unterstützung bedanken. Ohne euch und eure Unterstützung hätte ich nie die Möglichkeit gehabt dieses Studium erfolgreich durchzuführen. Ich weiß, dass ihr anfangs skeptisch wart, was ein Studium bei mir anging, dennoch habt ihr mich vom ersten Tag an, ohne nachzudenken, dabei unterstützt und geholfen. Die Chance die ihr mir gegeben habt werde ich euch nie zurückzahlen können. Und dafür möchte ich euch danken!

Als nächstes möchte ich mich bei Prof. Dr. Friedrich Aumayr bedanken. Du hast mir die Möglichkeit gegeben einen Einblick in die Fusionsforschung zu bekommen und dabei die Wichtigkeit dieses Forschungszweiges schätzen zu lernen. Auch hast Du mir die Chancen gegeben zu internationalen Konferenzen und Forschungseinrichtungen zu fahren um dort Erfahrungen zu sammeln und Kontakte mit Personen aus der ganzen Welt zu knüpfen. Ganz besonders möchte ich Dir auch danken, dass du mir -nicht nur während meiner Zeit in der Arbeitsgruppe, sondern auch in der Zeit, wo ich in deinen Vorlesungen als einfacher Student gesessen bin- neue und innovative Wege gezeigt hast, physikalische Probleme zu erkennen und diese dann auch zu lösen. Ich untertreibe nicht, wenn ich sage, dass meine Zeit in Deiner Arbeitsgruppe zu der schönsten Zeit meines Studiums gehört hat. Dein freundschaftliches Verhältnis und die Unterstützung, die Du mir gegeben hast, werde ich nicht vergessen!

Ein ganz spezieller Dank geht auch an Aileen. Du hast während der Zeit meines Masterstudiums alle Höhen und Tiefen, die ich während dieser Zeit durchgemacht habe mit mir überstanden und bist immer noch mit mir zusammen. Du hast mich immer unterstützt, sei es durch einfaches zuhören, wenn ich dir irgendwas über Physik erzählt habe oder mit mir aufregen, wenn ich mich über etwas aufregen musste. Für die Korrekturen bei dieser und vorangegangenen Arbeiten werde ich dir auch immer dankbar sein.

Weiteres möchte ich mich auch bei meinem direkten Betreuer Herrn Dipl.-Ing. Reinhard Stadlmayr bedanken. Ich weiß, dass wir anfangs nicht immer auf einer Wellenlänge waren. Die Herangehensweise an Problemstellungen ist bei uns leider sehr un-

terschiedlich. Dennoch finde ich, dass die Zeit, in der du mein Betreuer warst, eine sehr aufregende, tolle und gleichzeitig lehrreiche Zeit war! Du hast mir eine Vielzahl an Fähigkeiten beigebracht, deren Aufzählung hier zu viele wären. Ich möchte dir aber, von ganzem Herzen, Danke sagen.

Ein weiteres Dankeschön möchte ich auch an meine engsten Freunde entrichten, welche ich leider in den letzten Monaten meiner Arbeit viel zu sehr vernachlässigt habe. Danke, dass ihr mich in dieser Zeit unterstützt habt und immer an meiner Seite wart, wenn ich euch gebraucht habe ohne auf die vorrangegangenen Wochen/Monate des nicht Kontaktes zu reagieren oder mir böse gewesen zu sein. Ihr seid die Besten! Danke, Denise, Chris, Nici, René und vor allem Nicole & die Powerrangers.

Als letztes möchte ich mich noch bei meinen KollegInnen der Arbeitsgruppe bedanken. Besonders hervorgehoben sei hier Bernhard Berger. Danke, dass du während meiner Zeit als Projektstudent in der Arbeitsgruppe dich so aufopferungsvoll um meine Projektarbeit gekümmert hast. Ich habe dir Einiges zu verdanken, was das Schreiben von wissenschaftlichen Arbeiten angeht. Bei allen anderen Mitgliedern der Arbeitsgruppe, möchte ich mich natürlich auch bedanken. Da es so viel zu jedem zu sagen gäbe, die Danksagung jedoch nicht zu lange werden soll möchte ich dich Georg, Christian, Janine, Lorenz, Paul, David, Lukas, Florian, Elisabeth, Richard, Rimpei, Bernd und Martin namentlich erwähnen und mich für die tolle, lustige, sinnvolle, sinnlose, eigenartige, lehrreiche, freundschaftliche, investigative, nachtschwärmerische, singvolle, tanzvolle, ... Zeit bedanken. Ihr habt die Arbeitszeit und Freizeit zu einem wahrhaft tollen Erlebnis für mich gemacht.